Journal of Computational Physics 462 (2022) 111225

Contents lists available at ScienceDirect

Journal of Computational Physics

www.elsevier.com/locate/jcp

Finite volume method for coupled subsurface flow problems, II: Poroelasticity

Kirill M. Terekhov [a,b,*], Yuri V. Vassilevski [a,b,c]

[a] Marchuk Institute of Numerical Mathematics, Russian Academy of Sciences, Moscow, Russia
[b] Moscow Institute of Physics and Technology, Dolgoprydny, Russia
[c] Sechenov University, Moscow, Russia

ARTICLE INFO

Article history:
Received 11 October 2021
Received in revised form 23 March 2022
Accepted 10 April 2022
Available online 14 April 2022

Keywords:
Poromechanics
Poroelasticity
Full-tensor anisotropy
Heterogeneous media
Finite-volume

ABSTRACT

The article introduces a cell-centered finite-volume method for the Biot problem in heterogeneous anisotropic media, characterized with full-tensor properties. We derive the expression for the coupled flux and the interpolation method across the discontinuity of the properties. The obtained flux expression consists of a two-point part, a transversal part and an additional contribution due to gravity. The interpolation method is the generalization of the harmonic averaging point concept to coupled problems. The method is stable despite collocation of both pressure and displacement at cell centers due to eigensplitting of the matrix coefficients in the flux expression and upstream approximation. A general type of boundary condition is integrated without introduction of auxiliary degrees of freedom. Our flux discretization method is a realization of our more general concept of stable flux discretization for saddle-point systems with vector of several unknowns. We demonstrate the applicability of the method on a set of challenging numerical benchmarks.

1. Introduction

The poromechanics problem [1] is a multi-physics problem [2] addressing deformations of saturated porous media under load and accounting for mutual influence between structure movement and fluid flow [3,4]. Apart from the most popular application for predicting subsidence caused by oil recovery [5], the solutions of poroelastic problems are demanded in clay subsidence under load [6] or fluid drainage [7], earthquake impacts [8], drainage through blood vessels walls [9] etc. Most of applications deal with layered anisotropic media characterized by heterogeneous permeability tensor, compliance tensor and Biot tensor coefficient [10].

The most popular computational technologies within commercial and research poromechanical simulators [11] are based on a combination of the finite element method for the elasticity [12] and the finite volume method for the fluid flow [13,14]. Coupling between the two problems may be provided by the full spectrum of methods: from loose explicit to fully implicit approaches [15–18]. In the last decade a variety of new discretization methods have been suggested for the solution of the poroelastic problem, such as staggered finite-volume [19], mixed finite element [20], multipoint flux finite element [21]. The conservation property and implementation simplicity of the classical cell-centered finite volume method attracts growing attention [22] which is restricted, however, by possible inf-sup condition violation [23,24,22,25,26].

* Corresponding author at: Marchuk Institute of Numerical Mathematics, Russian Academy of Sciences, Moscow, Russia.
E-mail addresses: kirill.terehov@gmail.com (K.M. Terekhov), yuri.vassilevski@gmail.com (Yu.V. Vassilevski).

https://doi.org/10.1016/j.jcp.2022.111225
0021-9991/

The harmonic averaging point concept was introduced in [27] for the interpolation of pressure in the scalar anisotropic diffusion equation. The approach was extended in [28] to introduce the split definition of the flux for the same problem and further extended to elasticity problem [29], contact mechanics [30] and even poroelasticity [31]. Direct application to the latter resulted in an inf-sup unstable method.

The method presented in this paper follows our general strategy for the finite volume solution of multi-physics problems: (1) to avoid decoupling into sub-problems, and (2) to solve the problem in a locally conservative and fully implicit way via stable discretization of vector fluxes. This strategy allows us to work around the inconsistency of the FV method for poroelasticity appearing in heterogeneous media after decoupling of the Biot term from the Darcy flux. We assume the collocated arrangement of fluid pressure and structure displacement unknowns at cell centers and discretize the vector flux composed of the traction and Darcy/Biot fluxes.

The vector flux discretization for the poroelastic problem is a realization of our more general concept of stable two-point flux discretization of saddle-point systems with vector of several unknowns. Within this concept, FV approximation of the vector flux on a cell face is given by a linear combination of collocated at neighboring cell centers unknown vectors with matrix coefficients which have non-negative eigenvalues. To produce such matrix coefficients, one has to perform their eigensplitting. This concept was applied to cell-centered FV discretizations of the mixed formulation of the Darcy problem [26,32], the incompressible Navier-Stokes equations [32–34] and expressed in [30] for coupled problems in the context of the hydraulic fracturing problem. In case of scalar equations (e.g. diffusion equation) these matrix coefficients reduce to non-negative reals which guarantee monotone FV methods [32]. We note that flux matrix eigensplitting was exploited earlier for FV discretizations of Maxwell [35] and Navier-Stokes [36] equations on simple computational grids, and is also known in the literature as flux difference splitting and flux vector splitting [37], split upwinding [38].

In the numerical part, we verify efficiency and accuracy of the method on general grids for heterogeneous full-tensor permeability, compliance, and Biot coefficients by solving four benchmark problems. Applicability of the method to industrial grids with faults and pinch-outs is demonstrated for the solution of the poromechanical problem on Norne oil field with synthetic definition of stiffness tensor and Biot coefficient from permeability and porosity data of the original oil field.

The present work is the second paper in the series of papers devoted to ultimately stable fully coupled fully implicit FV discretizations of coupled subsurface problems. The first paper addresses the mixed formulation of the Darcy problem [26]. The present paper develops further the method proposed recently in [31] and benefits good stability properties according to the numerical evidence. Our method features simultaneously the cell-centered collocation of pressure and displacement, no LBB-related inconsistency and CFL-restrictions, handles general heterogeneous anisotropic tensor permeability, compliance, and Biot coefficients, general polyhedral meshes, general boundary conditions. Our extension of the harmonic point notion to the poromechanics problem in heterogeneous media is another important novelty of the paper.

The paper is organized as follows. In section 2 we introduce the poromechanical problem whose finite volume discretization method is given in section 3. In section 4 we derive the vector flux discretization and introduce the poroelastic harmonic point to cope with discontinuity of tensor coefficients across mesh faces. In section 5 we present the numerical tests. The concluding remarks finalize the paper.

2. Problem definition

We consider a 3D bulk polyhedral domain Ω composed of a solid porous matrix which is saturated by fluid. Given an appropriate initial condition, the linear poroelasticity problem in Ω is:

$$\begin{cases} -\mathbf{div}\,(\boldsymbol{\sigma} - \mathbb{B}p) = \rho g \nabla z + \mathbf{q}, \\ \dfrac{1}{M}\dfrac{\partial p}{\partial t} - \operatorname{div}\left(\dfrac{1}{\mu}\mathbb{K}\left(\nabla p - \rho_f g \nabla z\right)\right) + \mathbb{B} : \dfrac{\partial \boldsymbol{\epsilon}}{\partial t} = q, \\ \mathbf{S} : \boldsymbol{\sigma} = \boldsymbol{\epsilon}, \end{cases} \tag{1}$$

where **div** and div are vector and scalar divergences, $p \in H^1(\Omega)$ is the fluid pressure, $\mathbf{u} \in H^1(\Omega)^3$ is the solid displacement vector, $\boldsymbol{\sigma}$ is the 2-nd rank stress tensor, $\boldsymbol{\epsilon} = (\nabla \mathbf{u}^T + \mathbf{u}\nabla^T)/2$ is the 2-nd rank strain tensor, g is the gravitational constant, ϕ is the porosity, μ is the viscosity, ρ_f is the fluid density, ρ_s is the solid density, $\rho = \rho_f\phi + \rho_s(1-\phi)$ is the average density, $\mathbf{q}$ is the volumetric body force, q is the fluid source or sink. The piecewise constant media properties are defined by the symmetric 2-nd rank permeability tensor (matrix of order 3) $\mathbb{K}$, the symmetric 2-nd rank Biot coefficient tensor (matrix of order 3) $\mathbb{B}$, the Biot modulus M, and the 4-th rank elasticity compliance tensor (matrix of order 3 of matrices of order 3) $\mathbf{S}$.

The general form of boundary conditions on the domain boundary $\partial\Omega$ is:

$$\begin{cases} \mathbf{n}^T(\alpha_\perp \mathbf{u} - \beta_\perp \mathbf{t}_{\mathbb{B}}) = \gamma_\perp, \\ \left(\mathbb{I} - \mathbf{n}\mathbf{n}^T\right)(\alpha_\parallel \mathbf{u} - \beta_\parallel \mathbf{t}_{\mathbb{B}}) = \boldsymbol{\gamma}_\parallel, \\ \alpha_f p - \beta_f d = \gamma_f, \end{cases} \tag{2}$$

where $\mathbb{I}$ is the identity matrix of appropriate order, $\mathbf{n}$ is the unit outward normal vector to $\partial\Omega$, vector $\mathbf{t}_{\mathbb{B}}$ and scalar d are defined in (9). Different combinations of parameters $\alpha_\perp$, $\beta_\perp$, $\gamma_\perp$, $\alpha_\parallel$, $\beta_\parallel$, $\boldsymbol{\gamma}_\parallel$, α_f, β_f, γ_f impose different physics of the boundary conditions. In particular,

- $\alpha_\perp$ and $\beta_\perp$ define Dirichlet, Neumann or Robin boundary conditions for the normal component in the mechanical part with reaction $\gamma_\perp$;
- $\alpha_\parallel$ and $\beta_\parallel$ define Dirichlet, Neumann or Robin boundary conditions for the transversal components in the mechanical part with reaction $\boldsymbol{\gamma}_\parallel$;
- α_f and β_f define Dirichlet, Neumann or Robin boundary condition for the fluid flow with source γ_f.

The Biot term contribution to the Darcy flux can be reformulated as follows

$$\mathbb{B} : \frac{\partial \boldsymbol{\epsilon}}{\partial t} = \operatorname{div}\left(\mathbb{B}\frac{\partial \mathbf{u}}{\partial t}\right) - (\mathbb{B}\nabla)^T \frac{\partial \mathbf{u}}{\partial t}. \tag{3}$$

The elasticity compliance tensor $\mathbf{S}$ is assumed to be non-singular, *i.e.* the rock is compressible and the elasticity stiffness tensor $\mathbf{C} = \mathbf{S}^{-1}$ is well-defined and thus the stress-strain relation is known:

$$\boldsymbol{\sigma} = \mathbf{C} : \boldsymbol{\epsilon}. \tag{4}$$

The ij-th component of the stress tensor $\boldsymbol{\sigma}$ is expressed by:

$$\boldsymbol{\sigma}_{ij} = [\mathbf{C} : \boldsymbol{\epsilon}]_{ij} = \frac{1}{2}\begin{bmatrix} 2c_{ij11} & c_{ij12}+c_{ij21} & c_{ij13}+c_{ij31} \\ c_{ij12}+c_{ij21} & 2c_{ij22} & c_{ij23}+c_{ij32} \\ c_{ij13}+c_{ij31} & c_{ij23}+c_{ij32} & 2c_{ij33} \end{bmatrix} : \nabla \mathbf{u}^T = \mathbf{c}_{ij}^T (\mathbf{u} \otimes \nabla), \tag{5}$$

where $\otimes$ is the Kronecker product, $\mathbf{c}_{i,j}$ and $\mathbf{u} \otimes \nabla$ are vectors of order 9:

$$\mathbf{c}_{ij} = \frac{1}{2}\begin{bmatrix} 2c_{ij11} \\ c_{ij12}+c_{ij21} \\ c_{ij13}+c_{ij31} \\ c_{ij12}+c_{ij21} \\ 2c_{ij22} \\ c_{ij23}+c_{ij32} \\ c_{ij13}+c_{ij31} \\ c_{ij23}+c_{ij32} \\ 2c_{ij33} \end{bmatrix}, \quad \mathbf{u} \otimes \nabla = \begin{bmatrix} \nabla u \\ \nabla v \\ \nabla w \end{bmatrix} = \begin{bmatrix} \partial u/\partial x \\ \partial u/\partial y \\ \partial u/\partial z \\ \partial v/\partial x \\ \partial v/\partial y \\ \partial v/\partial z \\ \partial w/\partial x \\ \partial w/\partial y \\ \partial w/\partial z \end{bmatrix}. \tag{6}$$

3. Finite volume method

We assume that the domain Ω is covered by a consistent polyhedral mesh and denote by $\mathcal{V}(\Omega)$ the set of its cells, and by $\mathcal{F}(V)$ the set of faces for each cell $V \in \mathcal{V}(\Omega)$. Integrating equations (1) with relation (4) and expansion (3) over cell $V \in \mathcal{V}(\Omega)$ and using Gauss formula yield

$$\begin{cases} -\oint\limits_{\partial V} (\mathbf{C} : \boldsymbol{\epsilon} - \mathbb{B}p)\, \mathrm{d}\mathbf{S} = \int\limits_V (\rho g \nabla z + \mathbf{q})\, dV \\ -\oint\limits_{\partial V} \left(\frac{1}{\mu}\mathbb{K}(\nabla p - \rho g \nabla z) - \mathbb{B}\frac{\partial \mathbf{u}}{\partial t}\right)^T \mathrm{d}\mathbf{S} = \int\limits_V \left(q - \frac{1}{M}\frac{\partial p}{\partial t} + (\mathbb{B}\nabla)^T \frac{\partial \mathbf{u}}{\partial t}\right) \mathrm{d}V. \end{cases} \tag{7}$$

The second order quadrature for the approximation of the surface integrals in (7) reads as

$$\begin{aligned} -\oint\limits_{\partial V} (\mathbf{C} : \boldsymbol{\epsilon} - \mathbb{B}p)\, \mathrm{d}\mathbf{S} &\approx -\sum_{f \in \mathcal{F}(V)} |f|\, (\mathbf{C} : \boldsymbol{\epsilon} - \mathbb{B}p)|_{\mathbf{x}_f}\, \mathbf{n}, \\ -\oint\limits_{\partial V} \left(\frac{1}{\mu}\mathbb{K}\left(\nabla p - \rho_f g \nabla z\right) - \mathbb{B}\frac{\partial \mathbf{u}}{\partial t}\right)^T \mathrm{d}\mathbf{S} &\approx -\sum_{f \in \mathcal{F}(V)} |f| \left(\frac{1}{\mu}\mathbb{K}\left(\nabla p - \rho_f g \nabla z\right) - \mathbb{B}\frac{\partial \mathbf{u}}{\partial t}\right)^T \Bigg|_{\mathbf{x}_f} \mathbf{n}, \end{aligned} \tag{8}$$

where $|f|$ is the area of face f, $\mathbf{x}_f$ is the center of f, and $\mathbf{n}$ is the normal to f oriented outwards of V. The above formulation employs vector $\mathbf{t}_{\mathbb{B}}$ and scalar $d_{\mathbb{B}}$ which are the internal traction vector $\mathbf{t}$ and the Darcy flux d both augmented with the Biot terms as they appear in (8):

$$\mathbf{t} = -\boldsymbol{\sigma}\mathbf{n} = -\mathbf{C} : \boldsymbol{\epsilon}\,\mathbf{n}, \quad \mathbf{t}_{\mathbb{B}} = \mathbf{t} + \mathbb{B}p\mathbf{n}, \qquad d = -\frac{1}{\mu}\mathbf{n}^T\mathbb{K}\left(\nabla p - \rho_f g \nabla z\right), \quad d_{\mathbb{B}} = d + \mathbf{n}^T\mathbb{B}\frac{\partial \mathbf{u}}{\partial t}. \tag{9}$$

Using (5) and (6), we introduce the i-th component of the traction vector $\mathbf{t}$:

$$\mathbf{t}_i = -\boldsymbol{\sigma}_{i1}n_x - \boldsymbol{\sigma}_{i2}n_y - \boldsymbol{\sigma}_{i3}n_z = -\mathbf{n}^T \begin{bmatrix} \mathbf{c}_{i1}^T \\ \mathbf{c}_{i2}^T \\ \mathbf{c}_{i3}^T \end{bmatrix} \mathbf{u} \otimes \nabla, \tag{10}$$

then the full traction vector is given by

$$\mathbf{t} = \begin{bmatrix} \mathbf{t}_1 \\ \mathbf{t}_2 \\ \mathbf{t}_3 \end{bmatrix} = -\left(\mathbb{I} \otimes \mathbf{n}^T\right)\mathbb{C}\left(\mathbf{u} \otimes \nabla\right), \tag{11}$$

where the 9×9 matrix $\mathbb{C}$ is:

$$\mathbb{C} = \frac{1}{2}\begin{bmatrix}
2c_{1111} & c_{1112}+c_{1121} & c_{1113}+c_{1131} & c_{1112}+c_{1121} & 2c_{1122} & c_{1123}+c_{1132} & c_{1113}+c_{1131} & c_{1123}+c_{1132} & 2c_{1133} \\
2c_{1211} & c_{1212}+c_{1221} & c_{1213}+c_{1231} & c_{1212}+c_{1221} & 2c_{1222} & c_{1223}+c_{1232} & c_{1213}+c_{1231} & c_{1223}+c_{1232} & 2c_{1233} \\
2c_{1311} & c_{1312}+c_{1321} & c_{1313}+c_{1331} & c_{1312}+c_{1321} & 2c_{1322} & c_{1323}+c_{1332} & c_{1313}+c_{1331} & c_{1323}+c_{1332} & 2c_{1333} \\
2c_{2111} & c_{2112}+c_{2121} & c_{2113}+c_{2131} & c_{2112}+c_{2121} & 2c_{2122} & c_{2123}+c_{2132} & c_{2113}+c_{2131} & c_{2123}+c_{2132} & 2c_{2133} \\
2c_{2211} & c_{2212}+c_{2221} & c_{2213}+c_{2231} & c_{2212}+c_{2221} & 2c_{2222} & c_{2223}+c_{2232} & c_{2213}+c_{2231} & c_{2223}+c_{2232} & 2c_{2233} \\
2c_{2311} & c_{2312}+c_{2321} & c_{2313}+c_{2331} & c_{2312}+c_{2321} & 2c_{2322} & c_{2323}+c_{2332} & c_{2313}+c_{2331} & c_{2323}+c_{2332} & 2c_{2333} \\
2c_{3111} & c_{3112}+c_{3121} & c_{3113}+c_{3131} & c_{3112}+c_{3121} & 2c_{3122} & c_{3123}+c_{3132} & c_{3113}+c_{3131} & c_{3123}+c_{3132} & 2c_{3133} \\
2c_{3211} & c_{3212}+c_{3221} & c_{3213}+c_{3231} & c_{3212}+c_{3221} & 2c_{3222} & c_{3223}+c_{3232} & c_{3213}+c_{3231} & c_{3223}+c_{3232} & 2c_{3233} \\
2c_{3311} & c_{3312}+c_{3321} & c_{3313}+c_{3331} & c_{3312}+c_{3321} & 2c_{3322} & c_{3323}+c_{3332} & c_{3313}+c_{3331} & c_{3323}+c_{3332} & 2c_{3333}
\end{bmatrix}. \tag{12}$$

For time discretization, we shall use the stable Backward-Euler scheme

$$\frac{\partial p}{\partial t} \approx \frac{p^{n+1} - p^n}{\Delta t}, \quad \frac{\partial \mathbf{u}}{\partial t} \approx \frac{\mathbf{u}^{n+1} - \mathbf{u}^n}{\Delta t}. \tag{13}$$

We further use $\tau := \Delta t^{-1}$ and for briefness omit the next time step indices, $p := p^{n+1}, \mathbf{u} := \mathbf{u}^{n+1}$. Coupling together $\mathbf{t}_{\mathbb{B}}$ and $d_{\mathbb{B}}$ in (9), using the implicit time discretization (13), and using the reformulation (11), (12) of the internal traction vector $\mathbf{t}$ we arrive at the vector flux

$$\begin{bmatrix} \mathbf{t}_{\mathbb{B}} \\ d_{\mathbb{B}} \end{bmatrix} = -\mathbb{I} \otimes \mathbf{n}^T \begin{bmatrix} \mathbb{C} & \\ & \frac{1}{\mu}\mathbb{K} \end{bmatrix} \begin{bmatrix} \mathbf{u} \\ p \end{bmatrix} \otimes \nabla + \begin{bmatrix} & \mathbb{B}\mathbf{n} \\ \tau\mathbf{n}^T\mathbb{B} & \end{bmatrix} \begin{bmatrix} \mathbf{u} \\ p \end{bmatrix} + \begin{bmatrix} \\ \frac{1}{\mu}\rho g \mathbf{n}^T\mathbb{K}\nabla z - \tau\mathbf{n}^T\mathbb{B}\mathbf{u}^n \end{bmatrix}. \tag{14}$$

We use degrees of freedom collocated at cell centers: one fluid pressure p and three components u, v, w of displacement $\mathbf{u}$ per cell. Applying the simplest quadrature for approximation of the cell volume and cell face integrals we arrive at the finite volume formulation of (1):

$$\sum_{f \in \mathcal{F}(V)} |f| \begin{bmatrix} \mathbf{t}_{\mathbb{B}} \\ d_{\mathbb{B}} \end{bmatrix}\Big|_{\mathbf{x}_f} = |V| \begin{bmatrix} \rho g \nabla z + \mathbf{q} \\ q - \tau\left(p - p^n\right)/M + \tau\left(\mathbb{B}\nabla\right)^T\left(\mathbf{u} - \mathbf{u}^n\right) \end{bmatrix}\Big|_{\mathbf{x}_V}, \tag{15}$$

where $|V|$ and $\mathbf{x}_V$ are the volume and the center of cell V, respectively.

The discrete vector fluxes are derived in the next section. Since all the further derivations are performed on the flux level and the internal fluxes are unique on each interior face, the method is conservative [38]. Assembling the equation (15) over each cell $V \in \mathcal{V}(\Omega)$ we get a linear system to be solved for pressure and displacement unknowns. In the present work, the term $\mathbb{B}\nabla = \mathbf{0}$. If $\mathbb{B}$ is a solution-dependent tensorial piecewise-constant function, the term with $\mathbb{B}\nabla = \begin{bmatrix} \frac{\partial \mathbb{B}}{\partial u} & \frac{\partial \mathbb{B}}{\partial v} & \frac{\partial \mathbb{B}}{\partial w} & \frac{\partial \mathbb{B}}{\partial p} \end{bmatrix} \begin{bmatrix} \mathbf{u} \\ p \end{bmatrix} \otimes \nabla$ has to be retained.

4. Flux discretization

4.1. One-sided flux

We consider a cell $V_1 \in \mathcal{V}(\Omega)$ with center $\mathbf{x}_1$, an adjacent face $f \in \mathcal{F}(V_1)$ with center $\mathbf{x}_f$, the normal $\mathbf{n}$ oriented outwards, and denote by r_1 the distance from the cell center to the face $r_1 = \mathbf{n}^T(\mathbf{x}_f - \mathbf{x}_1) > 0$.

Assumption 1. In a vicinity of face f the discrete displacement and discrete pressure may be recovered from the collocated values $\mathbf{u}_1$ and p_1 to a continuous piecewise linear vector and scalar functions $\mathbf{u}$ and p, respectively: $\mathbf{u}_1 = \mathbf{u}|_{\mathbf{x}_1}$, $p_1 = p|_{\mathbf{x}_1}$.

Restrictions of $\mathbf{u}$ and p to the face center are $\mathbf{u}_f = \mathbf{u}|_{\mathbf{x}_f}$ and $p_f = p|_{\mathbf{x}_f}$. Local continuity and linearity of $\mathbf{u}$ and p imply their piecewise-constant gradient $\begin{bmatrix}\mathbf{u}\\ p\end{bmatrix} \otimes \nabla$ and thus we can define

$$\begin{bmatrix}\mathbf{u}_1\\ p_1\end{bmatrix} \otimes \nabla := \left(\begin{bmatrix}\mathbf{u}\\ p\end{bmatrix} \otimes \nabla\right)\Big|_{V_1} = \left[\frac{\partial u}{\partial x}\ \frac{\partial u}{\partial y}\ \frac{\partial u}{\partial z}\ \frac{\partial v}{\partial x}\ \frac{\partial v}{\partial y}\ \frac{\partial v}{\partial z}\ \frac{\partial w}{\partial x}\ \frac{\partial w}{\partial y}\ \frac{\partial w}{\partial z}\ \frac{\partial p}{\partial x}\ \frac{\partial p}{\partial y}\ \frac{\partial p}{\partial z}\right]^T\Big|_{V_1}. \tag{16}$$

Stiffness tensor $\mathbf{C}_1$, Biot coefficient tensor $\mathbb{B}_1$ and permeability tensor $\mathbb{K}_1$ are assumed to be constant in the cell V_1 with possible discontinuity across f.

Consider the V_1-sided approximation of (14) at face center $\mathbf{x}_f$

$$\begin{bmatrix}\mathbf{t}_{\mathbb{B}}\\ d_{\mathbb{B}}\end{bmatrix}\Big|_{\mathbf{x}_f} \approx -\mathbb{I} \otimes \mathbf{n}^T \begin{bmatrix}\mathbb{C}_1 & \\ & \frac{1}{\mu}\mathbb{K}_1\end{bmatrix}\begin{bmatrix}\mathbf{u}_1\\ p_1\end{bmatrix} \otimes \nabla + \begin{bmatrix} & \mathbb{B}_1\mathbf{n}\\ \tau\mathbf{n}^T\mathbb{B}_1 & \end{bmatrix}\begin{bmatrix}\mathbf{u}_f\\ p_f\end{bmatrix} + R_1, \tag{17}$$

where $R_1 = \begin{bmatrix}0 & 0 & 0 & \mu^{-1}\rho_f g\mathbf{n}^T\mathbb{K}_1\nabla z - \tau\mathbf{n}^T\mathbb{B}_1\mathbf{u}_f^n\end{bmatrix}^T$, value $\mathbf{u}_f^n$ is known from the previous time step or the initial condition.

For linear functions $\mathbf{u}$ and p we can split the gradient into the normal and transversal components

$$\begin{bmatrix}\mathbf{u}_1\\ p_1\end{bmatrix} \otimes \nabla = r_1^{-1}(\mathbb{I} \otimes \mathbf{n})\left(\begin{bmatrix}\mathbf{u}_f\\ p_f\end{bmatrix} - \begin{bmatrix}\mathbf{u}_1\\ p_1\end{bmatrix}\right) + \left(\mathbb{I} - r_1^{-1}\mathbb{I} \otimes \mathbf{n}\left(\mathbf{x}_f - \mathbf{x}_1\right)^T\right)\begin{bmatrix}\mathbf{u}_1\\ p_1\end{bmatrix} \otimes \nabla. \tag{18}$$

Introducing 4×12 and two 4×4 matrices

$$W_1 = \mathbb{I} \otimes \mathbf{n}^T \begin{bmatrix}\mathbb{C}_1 & \\ & \frac{1}{\mu}\mathbb{K}_1\end{bmatrix}, \quad B_1 = \begin{bmatrix} & \mathbb{B}_1\mathbf{n}\\ \tau\mathbf{n}^T\mathbb{B}_1 & \end{bmatrix}, \quad T_1 = r_1^{-1}W_1(\mathbb{I} \otimes \mathbf{n}), \tag{19}$$

and plugging (18), (19) into (17) we obtain the discretization of the vector flux

$$\begin{bmatrix}\mathbf{t}_{\mathbb{B}}\\ d_{\mathbb{B}}\end{bmatrix}\Big|_{\mathbf{x}_f} \approx T_1\begin{bmatrix}\mathbf{u}_1\\ p_1\end{bmatrix} - (T_1 - B_1)\begin{bmatrix}\mathbf{u}_f\\ p_f\end{bmatrix} + \left(T_1 \otimes \left(\mathbf{x}_f - \mathbf{x}_1\right)^T - W_1\right)\begin{bmatrix}\mathbf{u}_1\\ p_1\end{bmatrix} \otimes \nabla + R_1. \tag{20}$$

In (20), matrix $T_1 - B_1$ may have negative eigenvalues which are the source of numerical instability. The stabilized V_1-sided flux discretization is obtained by addition to (20) of the term

$$S_1\left(\begin{bmatrix}\mathbf{u}_1\\ p_1\end{bmatrix} - \begin{bmatrix}\mathbf{u}_f\\ p_f\end{bmatrix}\right) + S_1 \otimes \left(\mathbf{x}_f - \mathbf{x}_1\right)^T\begin{bmatrix}\mathbf{u}_1\\ p_1\end{bmatrix} \otimes \nabla, \tag{21}$$

with a 4×4 matrix S_1 to be defined later. Expression (21) vanishes for linear pressures and displacements, therefore the first order approximation of the vector flux is expected.

Lemma 1. *Let matrix S_1 be given by*

$$S_1 = \alpha_1\begin{bmatrix}b_1^{-1}\mathbb{B}_1\mathbf{n}\mathbf{n}^T\mathbb{B}_1 & \\ & b_1\end{bmatrix}, \tag{22}$$

with nonnegative parameter α_1 satisfying

$$\alpha_1 \geq \frac{\sqrt{(k_1 - c_1)^2 + 4b_1^2\tau} - (k_1 + c_1)}{2b_1}, \tag{23}$$

and parameters

$$b_1 = \sqrt{\mathbf{n}^T\mathbb{B}_1^2\mathbf{n}}, \quad c_1 = \frac{1}{r_1 b_1^2}\left(\mathbf{n}^T\mathbb{B}_1 \otimes \mathbf{n}^T\right)\mathbb{C}_1(\mathbf{n} \otimes \mathbb{B}_1\mathbf{n}), \quad k_1 = \frac{1}{r_1\mu}\mathbf{n}^T\mathbb{K}_1\mathbf{n}. \tag{24}$$

Then matrix $T_1 + S_1 - B_1$ has non-negative eigenvalues.

Proof. We introduce a 4×4 projection matrix P_1 and an auxiliary projected matrix $\hat{T}_1$:

$$P_1 = \begin{bmatrix}b_1^{-2}\mathbb{B}_1\mathbf{n}\mathbf{n}^T\mathbb{B}_1 & \\ & 1\end{bmatrix}, \quad \hat{T}_1 = P_1^T T_1 P_1 = \begin{bmatrix}c_1 b_1^{-2}\mathbb{B}_1\mathbf{n}\mathbf{n}^T\mathbb{B}_1 & \\ & k_1\end{bmatrix}, \tag{25}$$

where c_1 and k_1 are given in (24). Due to the projection and the symmetry of T_1 the property $T_1 - \hat{T}_1 \geq 0$ holds.

The direct computation of the eigenvalues of $\hat{T}_1 + S_1 - B_1$ using Maxima computer algebra package [39] yields

$$\lambda_{1,2} = \frac{1}{2}\left(k_1 + c_1 + 2\alpha_1 b_1 \pm \sqrt{(k_1 - c_1)^2 + 4b_1^2\tau}\right), \quad \lambda_{3,4} = 0. \tag{26}$$

Non-negativity of the eigenvalues in (26) implies (23) and hence eigenvalues of $T_1 + S_1 - B_1$ are non-negative. □

Remark 1. Symmetric matrix DB_1 with $D = \mathrm{diag}(1, 1, 1, \tau^{-1})$ is sign-indefinite with two non-zero eigenvalues $\pm b_1$. Splitting of DB_1 into two sign-definite matrices

$$DB_1 = \begin{bmatrix} & \mathbb{B}_1\mathbf{n} \\ \mathbf{n}^T\mathbb{B}_1 & \end{bmatrix} = \begin{bmatrix} -\sqrt{\tau}b_1^{-1}\mathbb{B}_1\mathbf{n}\mathbf{n}^T\mathbb{B}_1 & \mathbb{B}_1\mathbf{n} \\ \mathbf{n}^T\mathbb{B}_1 & -\frac{1}{\sqrt{\tau}}b_1 \end{bmatrix} + \begin{bmatrix} \sqrt{\tau}b_1^{-1}\mathbb{B}_1\mathbf{n}\mathbf{n}^T\mathbb{B}_1 & \\ & \frac{1}{\sqrt{\tau}}b_1 \end{bmatrix}, \tag{27}$$

motivates the choice of S_1 in (22). Indeed, ignoring contribution of $\hat{T}_1$ to $\hat{T}_1 + S_1 - B_1$ is equivalent to setting $k_1 = c_1 = 0$ in (23) and thus $DS_1 - DB_1 \geq 0$ for $\alpha_1 = \sqrt{\tau}$.

The final V_1-sided flux expression combining (20) and (21) reads as

$$\left[\begin{matrix}\mathbf{t}_{\mathbb{B}} \\ d_{\mathbb{B}}\end{matrix}\right]\Big|_{\mathbf{x}_f} \approx (T_1 + S_1)\begin{bmatrix}\mathbf{u}_1 \\ p_1\end{bmatrix} - (T_1 + S_1 - B_1)\begin{bmatrix}\mathbf{u}_f \\ p_f\end{bmatrix} + \left((T_1 + S_1)\otimes(\mathbf{x}_f - \mathbf{x}_1)^T - W_1\right)\begin{bmatrix}\mathbf{u}_1 \\ p_1\end{bmatrix}\otimes\nabla + R_1. \tag{28}$$

4.2. Flux in the bulk

We consider an internal face f shared by cells V_1 and V_2, with the normal $\mathbf{n}$ oriented towards V_2. Similarly to notations for cell V_1, pressure p_2 and displacement $\mathbf{u}_2$ are collocated at the center $\mathbf{x}_2$ of cell V_2, the distance from $\mathbf{x}_2$ to the face is given by $r_2 = \mathbf{n}^T(\mathbf{x}_2 - \mathbf{x}_f) > 0$. Tensors $\mathbb{K}_2$, $\mathbf{C}_2$ and $\mathbb{B}_2$ correspond to constant tensors of permeability, stiffness and Biot coefficient in cell V_2. Matrix $\mathbb{C}_2$ is a 9×9 matrix defined by the components of the stiffness tensor $\mathbf{C}_2$ according to (12).

Following the reasoning from section 4.1 we obtain the V_2-sided approximation of the vector flux at face f:

$$\left[\begin{matrix}\mathbf{t}_{\mathbb{B}} \\ d_{\mathbb{B}}\end{matrix}\right]\Big|_{\mathbf{x}_f} \approx (T_2 + S_2 - B_2)\begin{bmatrix}\mathbf{u}_f \\ p_f\end{bmatrix} - (T_2 + S_2)\begin{bmatrix}\mathbf{u}_2 \\ p_2\end{bmatrix} - \left((T_2 + S_2)\otimes(\mathbf{x}_f - \mathbf{x}_2)^T - W_2\right)\begin{bmatrix}\mathbf{u}_2 \\ p_2\end{bmatrix}\otimes\nabla - R_2, \tag{29}$$

with 4×12, and two 4×4 matrix coefficients

$$W_2 = -\mathbb{I}\otimes\mathbf{n}^T\begin{bmatrix}\mathbb{C}_2 & \\ & \frac{1}{\mu}\mathbb{K}_2\end{bmatrix}, \quad B_2 = -\begin{bmatrix}& \mathbb{B}_2\mathbf{n} \\ \tau\mathbf{n}^T\mathbb{B}_2 & \end{bmatrix}, \quad T_2 = -r_2^{-1}W_2(\mathbb{I}\otimes\mathbf{n}), \tag{30}$$

and $R_2 = \begin{bmatrix}0 & 0 & 0 & \tau\mathbf{n}^T\mathbb{B}_2\mathbf{u}_f^n - \mu^{-1}\rho_f g\mathbf{n}^T\mathbb{K}_2\nabla z\end{bmatrix}^T$. Definitions in (19) and (30) differ in the orientation of the normal: for cell V_2 the outward normal is $-\mathbf{n}$. The stabilizing matrix S_2 is independent of the normal orientation and is obtained by application of (22), (23), (24) to cell V_2.

Equating the one-sided approximations (28) and (29), we get an expression for the pressure and displacement at face f:

$$\begin{bmatrix}\mathbf{u}_f \\ p_f\end{bmatrix} = (T_1 + S_1 - B_1 + T_2 + S_2 - B_2)^{-1}\begin{pmatrix}(T_1 + S_1)\begin{bmatrix}\mathbf{u}_1 \\ p_1\end{bmatrix} + (T_2 + S_2)\begin{bmatrix}\mathbf{u}_2 \\ p_2\end{bmatrix} + R_1 + R_2 \\ + \left((T_1 + S_1)\otimes(\mathbf{x}_f - \mathbf{x}_1)^T - W_1\right)\begin{bmatrix}\mathbf{u}_1 \\ p_1\end{bmatrix}\otimes\nabla \\ + \left((T_2 + S_2)\otimes(\mathbf{x}_f - \mathbf{x}_2)^T - W_2\right)\begin{bmatrix}\mathbf{u}_2 \\ p_2\end{bmatrix}\otimes\nabla\end{pmatrix}. \tag{31}$$

Using (31) in either (28) or (29) we get the vector flux discretization based on the collocated at cell centers displacements and pressures and reconstructed gradients:

$$\begin{aligned}\left[\begin{matrix}\mathbf{t}_{\mathbb{B}} \\ d_{\mathbb{B}}\end{matrix}\right]\Big|_{\mathbf{x}_f} \approx{}& (T_2 + S_2 - B_2)(T_1 + S_1 - B_1 + T_2 + S_2 - B_2)^{-1} \\ &\times\left((T_1 + S_1)\begin{bmatrix}\mathbf{u}_1 \\ p_1\end{bmatrix} + \left((T_1 + S_1)\otimes(\mathbf{x}_f - \mathbf{x}_1)^T - W_1\right)\begin{bmatrix}\mathbf{u}_1 \\ p_1\end{bmatrix}\otimes\nabla + R_1\right) \\ &- (T_1 + S_1 - B_1)(T_1 + S_1 - B_1 + T_2 + S_2 - B_2)^{-1} \\ &\times\left((T_2 + S_2)\begin{bmatrix}\mathbf{u}_2 \\ p_2\end{bmatrix} + \left((T_2 + S_2)\otimes(\mathbf{x}_f - \mathbf{x}_2)^T - W_2\right)\begin{bmatrix}\mathbf{u}_2 \\ p_2\end{bmatrix}\otimes\nabla + R_2\right).\end{aligned} \tag{32}$$

The gradient reconstruction is discussed in section 4.4.

4.3. Flux through the boundary

Now we consider a boundary face $f = \partial\Omega \cap V_1$ with face center $\mathbf{x}_f$ and normal $\mathbf{n}$ oriented outside of the domain. The pressure p_1 and the displacement $\mathbf{u}_1$ are assumed to be collocated in the V_1-cell center $\mathbf{x}_1$. Conditions (2) are equivalent to the system

$$B_D \begin{bmatrix} \mathbf{u}_f \\ p_f \end{bmatrix} - B_N \begin{bmatrix} \mathbf{t}_{\mathbb{B}} \\ d \end{bmatrix}\Big|_{\mathbf{x}_f} = \mathbf{R}, \tag{33}$$

where

$$B_D = \begin{bmatrix} \alpha_\perp \mathbf{n}\mathbf{n}^T + \alpha_\parallel \left(\mathbb{I} - \mathbf{n}\mathbf{n}^T\right) & \\ & \alpha_f \end{bmatrix}, \; B_N = \begin{bmatrix} \beta_\perp \mathbf{n}\mathbf{n}^T + \beta_\parallel \left(\mathbb{I} - \mathbf{n}\mathbf{n}^T\right) & \\ & \beta_f \end{bmatrix}, \; \mathbf{R} = \begin{bmatrix} \gamma_\perp \mathbf{n} + \boldsymbol{\gamma}_\parallel \\ \gamma_f \end{bmatrix}. \tag{34}$$

Since d does not contain the Biot term, we write approximation of $[\mathbf{t}_{\mathbb{B}} \; d]^T$:

$$\begin{bmatrix} \mathbf{t}_{\mathbb{B}} \\ d \end{bmatrix}\Big|_{\mathbf{x}_f} \approx -\left(\mathbb{I} \otimes \mathbf{n}^T\right) \begin{bmatrix} \mathbb{C}_1 & \\ & \frac{1}{\mu}\mathbb{K}_1 \end{bmatrix} \begin{bmatrix} \mathbf{u}_1 \\ p_1 \end{bmatrix} \otimes \nabla + \begin{bmatrix} \mathbf{0}^T & \mathbb{B}_1 \mathbf{n} \end{bmatrix} \begin{bmatrix} \mathbf{u}_f \\ p_f \end{bmatrix} + \bar{R}_1, \tag{35}$$

where $\bar{R}_1 = \begin{bmatrix} 0 & 0 & 0 & \mu^{-1}\rho_f g \mathbf{n}^T \mathbb{K}_1 \nabla z \end{bmatrix}^T$. Using the gradient splitting (18) in (35) we get:

$$\begin{bmatrix} \mathbf{t}_{\mathbb{B}} \\ d \end{bmatrix}\Big|_{\mathbf{x}_f} \approx T_1 \begin{bmatrix} \mathbf{u}_1 \\ p_1 \end{bmatrix} - (T_1 - \bar{B}_1) \begin{bmatrix} \mathbf{u}_f \\ p_f \end{bmatrix} + \left(T_1 \otimes \left(\mathbf{x}_f - \mathbf{x}_1\right)^T - W_1\right) \begin{bmatrix} \mathbf{u}_1 \\ p_1 \end{bmatrix} \otimes \nabla + \bar{R}_1, \tag{36}$$

where

$$\bar{B}_1 = \begin{bmatrix} \mathbf{0}^T & \mathbb{B}_1 \mathbf{n} \end{bmatrix}. \tag{37}$$

Plugging (36) into (33) we get an expression for the pressure and displacement at face f:

$$\begin{aligned} \begin{bmatrix} \mathbf{u}_f \\ p_f \end{bmatrix} &= \left(B_D + B_N(T_1 - \bar{B}_1)\right)^{-1} \\ &\times \left(\mathbf{R} + B_N \left(T_1 \begin{bmatrix} \mathbf{u}_1 \\ p_1 \end{bmatrix} + \left(T_1 \otimes \left(\mathbf{x}_f - \mathbf{x}_1\right)^T - W_1\right) \begin{bmatrix} \mathbf{u}_1 \\ p_1 \end{bmatrix} \otimes \nabla + \bar{R}_1\right)\right). \end{aligned} \tag{38}$$

The vector flux discretization at the boundary is obtained by using (36), (38) and the reconstructed gradient.

4.4. Gradient reconstruction

The final discrete fluxes on internal (32) or boundary (38), (36) faces rely on the gradients to be reconstructed at each cell of the mesh. For each face $f \in \mathcal{F}(V_1)$ we shall define a harmonic point generating four linear equations for the unknown gradient. All faces from $\mathcal{F}(V_1)$ produce a system for unknown vector $\mathbf{g} = \begin{bmatrix} \mathbf{u}_1 & p_1 \end{bmatrix}^T \otimes \nabla \in \Re^{12}$ with a matrix $A \in \Re^{4|\mathcal{F}(V_1)| \times 12}$ and a vector $\mathbf{b} \in \Re^{4|\mathcal{F}(V_1)|}$

$$A\mathbf{g} = \mathbf{b}, \tag{39}$$

which is solved by the least-squares method $\mathbf{g} = (A^T A)^{-1} A^T \mathbf{b}$.

In order to reconstruct the gradient locally, for each face we have to find a harmonic point where local recovery of the collocated pressures and displacements does not use the reconstructed gradient and the system (39) makes sense. The harmonic point with displacement $\mathbf{u}_h$ and pressure p_h satisfies

$$\begin{bmatrix} \mathbf{u}_f \\ p_f \end{bmatrix} = \begin{bmatrix} \mathbf{u}_h \\ p_h \end{bmatrix} + \left(\mathbb{I} \otimes \mathbf{x}_f - X_h\right)^T \begin{bmatrix} \mathbf{u}_1 \\ p_1 \end{bmatrix} \otimes \nabla = \begin{bmatrix} \mathbf{u}_h \\ p_h \end{bmatrix} + \left(\mathbb{I} \otimes \mathbf{x}_f - X_h\right)^T \begin{bmatrix} \mathbf{u}_2 \\ p_2 \end{bmatrix} \otimes \nabla, \tag{40}$$

where X_h is a 4×4 matrix of vectors of order 3 given by

$$X_h = \mathbb{I} \otimes \mathbf{x}_f + \begin{bmatrix} \mathbf{t}_h^{uu} & \mathbf{t}_h^{uv} & \mathbf{t}_h^{uw} & \mathbf{t}_h^{up} \\ \mathbf{t}_h^{vu} & \mathbf{t}_h^{vv} & \mathbf{t}_h^{vw} & \mathbf{t}_h^{vp} \\ \mathbf{t}_h^{wu} & \mathbf{t}_h^{wv} & \mathbf{t}_h^{ww} & \mathbf{t}_h^{wp} \\ \mathbf{t}_h^{pu} & \mathbf{t}_h^{pv} & \mathbf{t}_h^{pw} & \mathbf{t}_h^{pp} \end{bmatrix}, \quad \left(\mathbb{I} - \mathbf{n}\mathbf{n}^T\right) \mathbf{t}_h^{\alpha\beta} = \mathbf{0}, \quad \forall \alpha, \beta \in \{u, v, w, p\}. \tag{41}$$

From the geometrical viewpoint, the vectors on the diagonal of X_h are coordinates on the plane of face f and the off-diagonal vectors are tangential to the plane of face f. Due to Assumption 1 the transversal components of the gradients are

continuous and vectors $\mathbf{t}_h^{\alpha\beta}$ in (41) are required to satisfy this in (40). The vectors $\mathbf{t}_h^{\alpha\beta}$ provide cancellation of the gradients when a combination of expressions in (40) is equated to (31). It turns out that the stabilization terms S_1, S_2 do not allow to cancel the gradient without violation of the geometrical constraints (41). Therefore, we repeat the same derivation of (31) without the stabilization terms S_1, S_2 and derive existence of a harmonic point

$$X_h^T = \mathbb{I} \otimes \mathbf{x}_f^T + (T_1 + T_2 - B_1 - B_2)^{-1} \left(T_1 \otimes \left(\mathbf{x}_1 - \mathbf{x}_f\right)^T + T_2 \otimes \left(\mathbf{x}_2 - \mathbf{x}_f\right)^T + W_1 + W_2 \right), \tag{42}$$

such that the gradient terms are canceled, and displacement and pressure admit the harmonic averaging:

$$\begin{bmatrix} \mathbf{u}_h \\ p_h \end{bmatrix} = (T_1 + T_2 - B_1 - B_2)^{-1} \left(T_1 \begin{bmatrix} \mathbf{u}_1 \\ p_1 \end{bmatrix} + T_2 \begin{bmatrix} \mathbf{u}_2 \\ p_2 \end{bmatrix} + R_1 + R_2 \right). \tag{43}$$

Now we consider a boundary face $f = \partial\Omega \cap V_1$. Using (40) and (38) we eliminate contribution of the gradient terms and get

$$X_h^T = \mathbb{I} \otimes \mathbf{x}_f^T + \left(B_D + B_N(T_1 - \bar{B}_1)\right)^{-1} B_N \left(W_1 - T_1 \otimes \left(\mathbf{x}_f - \mathbf{x}_1\right)^T \right), \tag{44}$$

so that

$$\begin{bmatrix} \mathbf{u}_h \\ p_h \end{bmatrix} = \left(B_D + B_N(T_1 - \bar{B}_1)\right)^{-1} \left(\mathbf{R} + B_N T_1 \begin{bmatrix} \mathbf{u}_1 \\ p_1 \end{bmatrix} + B_N \bar{R}_1 \right). \tag{45}$$

Each face from $\mathcal{F}(V_1)$ contributes to system (39) four equations

$$(X_h - \mathbb{I} \otimes \mathbf{x}_1)^T \begin{bmatrix} \mathbf{u}_1 \\ p_1 \end{bmatrix} \otimes \nabla = \begin{bmatrix} \mathbf{u}_h \\ p_h \end{bmatrix} - \begin{bmatrix} \mathbf{u}_1 \\ p_1 \end{bmatrix}, \tag{46}$$

where combinations of (42)-(43) and (44)-(45) are used on internal and boundary faces, respectively.

5. Numerical experiments

The solution of the problem consists in assembling and solving on each time step the linear system (15) with the fluxes defined by (32) on internal faces and combination of (38) and (28) on boundary faces. The gradients for the computation of fluxes are reconstructed as described in § 4.4. To evaluate the Biot term in the right hand side R_1 of the fluxes (28), we update the interface displacement at the end of each time step using (31) and (38) on internal and boundary faces, respectively. The initial interface displacement is restored from the initial cell-centered pressures and displacements using the same formulas with zero parameter τ.

Further, we define the elastic material properties in Voigt notation. A 6×6 matrix representation of an anisotropic compliance tensor $\mathbf{S}$ defined in terms of Young modulii E_x, E_y, E_z, Poisson ratios $\nu_{xy}, \nu_{xz}, \nu_{yz}$ and shear modulii G_{xy}, G_{xz}, G_{yz}, is

$$S = \begin{pmatrix} \frac{1}{E_x} & -\frac{\nu_{yx}}{E_y} & -\frac{\nu_{zx}}{E_z} & & & \\ -\frac{\nu_{xy}}{E_x} & \frac{1}{E_y} & -\frac{\nu_{zy}}{E_z} & & & \\ -\frac{\nu_{xz}}{E_x} & -\frac{\nu_{yz}}{E_y} & \frac{1}{E_z} & & & \\ & & & \frac{1}{2G_{yz}} & & \\ & & & & \frac{1}{2G_{xz}} & \\ & & & & & \frac{1}{2G_{xy}} \end{pmatrix}. \tag{47}$$

Due to the symmetry it holds $\nu_{yx} = E_y \nu_{xy}/E_x$, $\nu_{zx} = E_z \nu_{xz}/E_x$, $\nu_{zy} = E_z \nu_{yz}/E_y$ and thus S has 9 independent parameters. For transversely isotropic material in Oxy direction it holds $E_y = E_x$, $\nu_{xz} = \nu_{yz}$, $G_{xy} = \frac{E_x}{2(1+\nu_{xy})}$, $G_{yz} = G_{xz}$ and the material is described by 5 independent parameters E_x, E_z, ν_{xy}, ν_{xz}, G_{xz}. For isotropic material it holds $E_x = E_y = E_z = E$, $\nu_{xy} = \nu_{xz} = \nu_{yz} = \nu$, $G_{xy} = G_{xz} = G_{yz} = \frac{E}{2(1+\nu)}$ and the material is described by 2 independent parameters E, ν. The stiffness tensor $\mathbf{C}$ in Voigt notation is given by a 6×6 matrix $C = S^{-1}$ which is related to the 9×9 matrix $\mathbb{C}$ (12) via

$$\mathbb{C} = BCB^T, \quad B^T = \begin{bmatrix} 1 & 0 & 0 & 0 & 0 & 0 & 0 & 0 & 0 \\ 0 & 0 & 0 & 0 & 1 & 0 & 0 & 0 & 0 \\ 0 & 0 & 0 & 0 & 0 & 0 & 0 & 0 & 1 \\ 0 & 0 & 0 & 0 & 0 & 1 & 0 & 1 & 0 \\ 0 & 0 & 1 & 0 & 0 & 0 & 1 & 0 & 0 \\ 0 & 1 & 0 & 1 & 0 & 0 & 0 & 0 & 0 \end{bmatrix}. \tag{48}$$

The types of used mechanical boundary conditions are listed in Table 1: Dirichlet condition Γ_D^m defines the boundary displacement $\mathbf{u}$, Neumann boundary condition Γ_N^m defines the applied force $\mathbf{F}$, the roller boundary condition Γ_R^m fixes

Table 1
Parameters of boundary conditions of different types.

Type	$\alpha_\perp$	$\beta_\perp$	$\alpha_\parallel$	$\beta_\parallel$	$\gamma_\perp$	$\gamma_\parallel$
Γ_D^m	1	0	1	0	$\mathbf{n}^T\mathbf{u}_b$	$(\mathbb{I}-\mathbf{n}\mathbf{n}^T)\,\mathbf{u}_b$
Γ_N^m	0	1	0	1	$\mathbf{n}^T\mathbf{F}$	$(\mathbb{I}-\mathbf{n}\mathbf{n}^T)\,\mathbf{F}$
Γ_R^m	1	0	0	1	0	$\mathbf{0}$
Γ_{RP}^m	1	0	0	1	λ	$\mathbf{0}$
Γ_T^m	0	1	1	0	0	$\mathbf{0}$

displacements in the normal direction and releases displacements in the transversal direction, the rigid plate boundary condition Γ_{RP}^m, constrains vertical displacement by a Lagrange multiplier λ, the pushing boundary condition Γ_T^m fixes displacements in the transversal direction and releases displacements in the normal direction. The types of fluid boundary conditions are: Dirichlet condition Γ_D^f imposes pressure with parameters $\alpha_f = 1$, $\beta_f = 0$, $\gamma_f = p_b$, and Neumann condition Γ_N^f imposes impermeable wall with parameters $\alpha_f = 0$, $\beta_f = 1$, $\gamma_f = 0$.

In the absence of the gravity, the problem is independent of porosity ϕ, solid density ρ_s and fluid density ρ_f.

The L_2-integral error norms for the discrete displacements $\mathbf{u}_i$ and pressures p_i are computed as follows:

$$\varepsilon_{\mathbf{u}} := \sqrt{\frac{1}{|\Omega|}\sum_{V_i\in\mathcal{V}(\Omega)} |V_i|\left(\mathbf{u}_i - \mathbf{u}|_{\mathbf{x}_i}\right)^T\left(\mathbf{u}_i - \mathbf{u}|_{\mathbf{x}_i}\right)}, \quad \varepsilon_p := \sqrt{\frac{1}{|\Omega|}\sum_{V_i\in\mathcal{V}(\Omega)} |V_i|\left(p_i - p|_{\mathbf{x}_i}\right)^2}, \tag{49}$$

where $\mathbf{u}$ and p are exact displacement and pressure solutions.

The numerical experiments are based on INMOST toolkit for distributed mathematical modeling [32,40–43] which provides tools for mesh handling, linear system assembly via automatic differentiation, linear system solution, and visualization. We solve arising linear systems iteratively using the BiConjugate Stabilized Gradient method [44] with the second-order [45] Crout-ILU [46] multilevel preconditioner [47]. The preconditioner features an adaptive dropping strategy based on estimation of the condition number of the inverse factors [48] and maximum product transversal preordering [49]. The absolute tolerance of the iterative solver is 10^{-10}, the relative tolerance is 10^{-16}. The dropping tolerances are $\tau_1 = 10^{-2}$, $\tau_2 = 10^{-3}$, the condition estimator threshold for deferred pivoting is $\kappa = 2.5$. For the parallel run in § 5.8 we set two overlapping layers in the additive Schwarz method.

5.1. Linear analytical solution in general anisotropic medium

Consider a problem in the unit cube $\Omega = [0,1]^3$ with the following stiffness tensor in Voigt notation:

$$C = \begin{pmatrix} 93 & 46 & 22 & 13 & 72 & 35 \\ 46 & 95 & 41 & 62 & 56 & 24 \\ 22 & 41 & 89 & 25 & 33 & 21 \\ 13 & 62 & 25 & 87 & 13 & 25 \\ 72 & 56 & 33 & 13 & 99 & 57 \\ 35 & 24 & 21 & 25 & 57 & 78 \end{pmatrix}. \tag{50}$$

The homogeneous anisotropic Biot tensor and the permeability tensor are given as follows:

$$\mathbb{B} = \frac{1}{100}\begin{pmatrix} 1 & 6 & 5 \\ 6 & 67 & 27 \\ 5 & 27 & 76 \end{pmatrix}, \quad \mathbb{K} = \frac{1}{1000}\begin{pmatrix} 25 & 2 & 39 \\ 2 & 42 & 7 \\ 39 & 7 & 100 \end{pmatrix}. \tag{51}$$

The eigenvalues of C, $\mathbb{B}$ and $\mathbb{K}$ are positive. The fluid parameters are the viscosity $\mu = 0.1$ and the Biot modulus $M = 0.1$. The gravity is absent, $g = 0$. The time step is $\Delta t = 1$ is equal to the total simulation time $T = 1$.

The analytical solution

$$\begin{bmatrix} \mathbf{u} \\ p \end{bmatrix} = \begin{bmatrix} u \\ v \\ w \\ p \end{bmatrix} = \begin{bmatrix} 1 & 2 & 3 & 4 \\ 6 & 7 & 8 & 9 \\ 11 & 12 & 13 & 14 \\ 16 & 17 & 18 & 19 \end{bmatrix}\begin{bmatrix} x \\ y \\ z \\ t \end{bmatrix} + \begin{bmatrix} 5 \\ 10 \\ 15 \\ 20 \end{bmatrix} \tag{52}$$

produces the right-hand sides $\mathbf{q} = (2.08, 17.21, -1780.93)^T$ and $q = 190$. We set Dirichlet conditions $\Gamma_D^m \cup \Gamma_D^f$ with $\mathbf{u}_b = \mathbf{u}(\mathbf{x}, t)$ and $p_b = p(x, t)$ on the entire boundary $\partial\Omega$. The initial conditions are given by the reference solution. The Biot term in the fluid equation accounting for the pore expansion effect vanishes in this setup.

The problem is solved on a regular cubic and tetrahedral grids displayed in Fig. 1. The error norms are given in Table 2. The method is exact for the linear solution and handles a general anisotropic material.

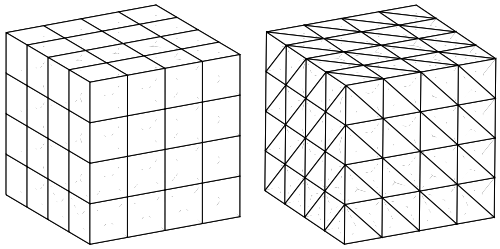

Fig. 1. Grids used for the test in § 5.1.

Table 2
Error norms computed for the test in § 5.1.

Mesh	$\lvert\mathcal{V}(\Omega)\rvert$	ε_u	ε_p
cubic	64	7.59e-13	1.69e-12
tetrahedral	384	3.16e-13	1.99e-12

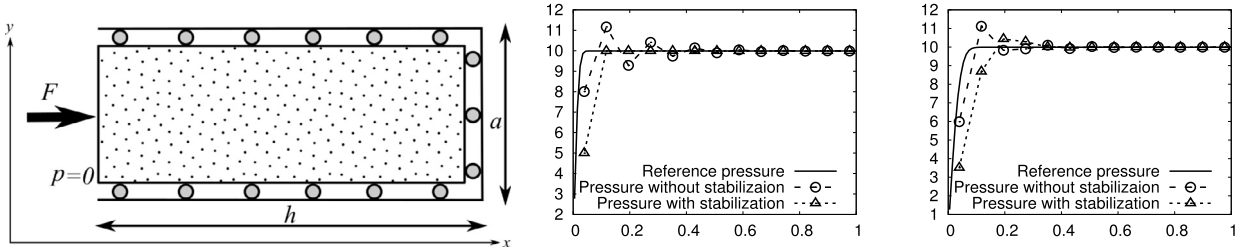

Fig. 2. Setup of Terzaghi's column consolidation problem (left) in § 5.2. Action of the stabilization method with $128 \times 1 \times 1$ grid and time step $\Delta t = 100$ at $T = 100$ (middle) and $T = 500$ (right), horizontal axis corresponds to coordinate $x \in [0, 1]$, vertical axis corresponds to fluid pressure.

5.2. Terzaghi's problem

Consider one-dimensional problem for consolidation under constant load F of a column of height h, see Fig. 2. The exact solution [50] (page 124) and [51] is

$$\begin{aligned} u(x,t) &= \frac{F(h-x)(1-2\nu)}{2G(1-\nu)} \\ &\quad - \frac{4Fh(\nu_u-\nu)}{\pi^2 G(1-\nu)(1-\nu_u)} \sum_{m=0}^{\infty} \frac{1}{(1+2m)^2} \exp\left(-(1+2m)^2 \frac{\pi^2 ct}{4h^2}\right) \cos\left((1+2m)\frac{\pi x}{2h}\right), \\ p(x,t) &= \frac{FB(1+\nu_u)}{3(1-\nu_u)} \\ &\quad - \frac{FB(1+\nu_u)}{3(1-\nu_u)} \sum_{m=0}^{\infty} (-1)^m \left(\operatorname{erfc}\left(\frac{(1+2m)h-(x-h)}{\sqrt{4ct}}\right) + \operatorname{erfc}\left(\frac{(1+2m)h+(x-h)}{\sqrt{4ct}}\right)\right), \end{aligned} \tag{53}$$

where α is the Biot coefficient, E is the Young modulus, ν is the Poisson's ratio, G is the shear modulus, c is the consolidation coefficient, ν_u is the undrained Poisson's ratio, B is Skempton's coefficient. The parameters of the isotropic medium are collected in Table 3. The above coefficients are given by

$$G = \frac{E}{2(1+\nu)}, \quad c = \frac{2kG(1-\nu)(\nu_u-\nu)}{\mu\alpha^2(1-\nu_u)(1-2\nu)^2}, \quad \nu_u = \frac{3\nu+\alpha B(1-2\nu)}{3-\alpha B(1-2\nu)}, \quad B = \frac{3\alpha(1-2\nu)M}{E+3\alpha^2(1-2\nu)M}. \tag{54}$$

The initial conditions are

$$u(x,0) = \frac{F(h-x)(1-2\nu_u)}{2G(1-\nu_u)}, \quad p(x,0) = \frac{FB(1+\nu_u)}{3(1-\nu_u)}. \tag{55}$$

The boundary conditions $\Gamma_N^m \cup \Gamma_D^f$ with force $\mathbf{F} = (F, 0, 0)^T$ and $p_b = 0$ are imposed at $\partial\Omega \cap \{x = 0\}$. The rest of the boundary corresponds to the impermeable roller boundary condition $\Gamma_R^m \cup \Gamma_N^f$, see Fig. 2 (left). The size of the box is $h = 10$, $a = 1$, the applied force is $F = 10$. A pseudo one-dimensional cubic grid of size $N \times 1 \times 1$ is used in this test. The total

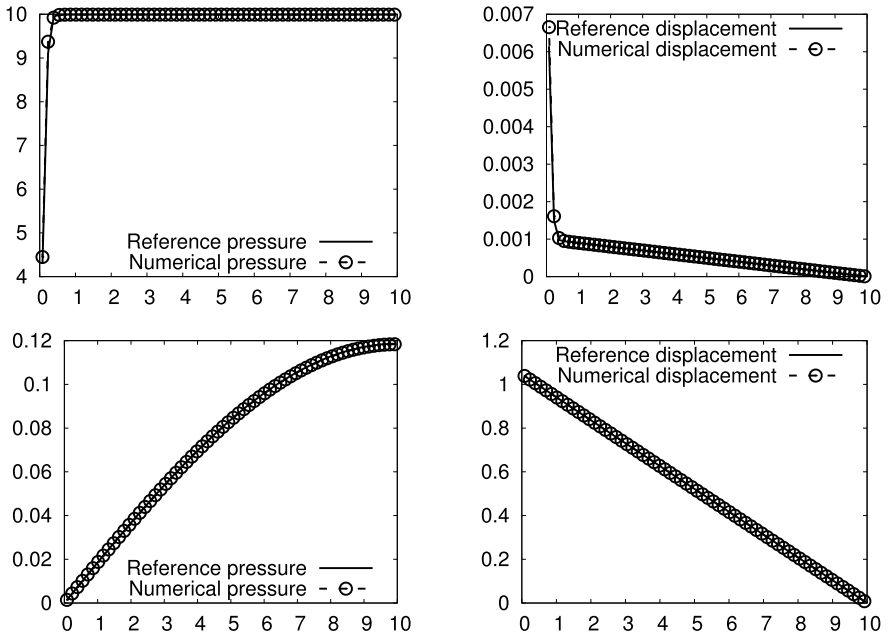

Fig. 3. Pressure (left) and displacement (right) at vertical axis against coordinate $x \in [0, 10]$ at horizontal axis for Terzaghi's problem § 5.2 at time instants $T = 10000$ (top) and $T = 2 \cdot 10^8$ (bottom) on the $64 \times 1 \times 1$ grid with time step $\Delta t = 10^4$.

Table 3
Parameters in for the test in § 5.2.

E	ν	k	α	M	μ	g
25	0.45	10^{-11}	1	100000	10^{-3}	0

Table 4
Error norms at $T = 10000$ for the test in § 5.2.

Method:		stabilized		non-stabilized	
$\lvert\mathcal{V}(\Omega)\rvert$	Δt	ε_u	ε_p	ε_u	ε_p
$128 \times 1 \times 1$	100	3.1e-4	2.4e-1	4.0e-5	2.4e-2
$256 \times 1 \times 1$	50	6.3e-5	6.3e-2	9.7e-6	5.7e-3
$512 \times 1 \times 1$	25	8.1e-6	9.4e-3	2.3e-6	1.3e-3
rate	-	2.96	2.74	2.07	2.13

simulation time is $T = 10000$, which corresponds to a tiny fraction of the total consolidation time with the given parameters, see Fig. 3. In this problem, oscillations may develop in numerical methods at initial time steps due to abrupt change in the pressure near the boundary [52]. The impact of the stabilization method is illustrated on the coarse grid ($N = 128$, time step $\Delta t = 100$) at time $T = 100$ in Fig. 2 (middle) and at time $T = 500$ in Fig. 2 (right). The oscillations in the pressure are suppressed by the stabilization method. The solution with the stabilization method is found to contain a soft kink that slightly overshoots over the reference solution. Such effect is possibly caused by the contribution of the gradient terms to the flux. It can be addressed in the future work by approximating these gradient terms with a nonlinear finite volume method as in [28]. The convergence of the discrete solution is demonstrated in Table 4. In this test, according to Table 4, the oscillatory non-stabilized solution recovers in several steps and appears to be more accurate than the stabilized solution. The cause of this is the added dissipation of the stabilization method.

5.3. Mandel's problem

The original two-dimensional problem [53] is defined in the domain $[-a, a] \times [-b, b]$. The top and bottom sides at $y = \pm b$ are loaded by the vertical force $2F$ acting on rigid impermeable plates. The medium is isotropic. The left and right sides at $x = \pm a$ are free and permeable. The problem is symmetric with respect to $x = 0$ and $y = 0$. Due to its symmetry, the problem is solved in the 3D domain $\Omega = [0, a] \times [0, b] \times [0, a]$. The force F is applied through an impermeable rigid plate at the top side $y = b$. The analytical solution in terms of force F, consolidation coefficient c, Young modulus E, drained ν and undrained ν_u Poisson's ratios, shear modulus G and Skempton's pore pressure B (54) reads as

Table 5
Parameters for the test in § 5.3.

E	ν	k	α	M	μ	g
25	0.25	10^{-6}	1	10000	10^{-3}	0

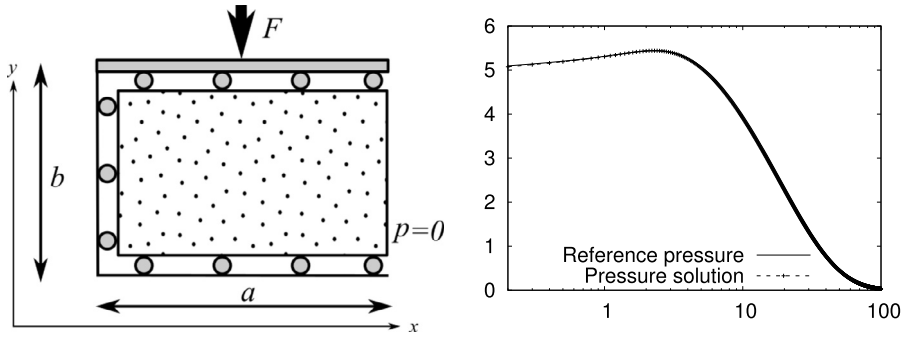

Fig. 4. Setup of Mandel's problem (left) in § 5.3. Reproduction of the Mandel-Cryer effect of non-monotone pressure behavior over time period $T = 100$ with $\Delta t = 0.1$ at the left side of the $8 \times 16 \times 1$ cubic mesh, horizontal axis corresponds to time in log scale, vertical axis corresponds to fluid pressure (right).

$$
\begin{aligned}
u(x,t) &= \frac{F}{Ga}\left(\frac{\nu x}{2} + \sum_{m=1}^{\infty}\left(a\sin\left(\frac{\omega_m x}{a}\right) - \nu_u x\sin(\omega_m)\right)\frac{\cos(\omega_m)}{\omega_m - \sin(\omega_m)\cos(\omega_m)}\exp\left(\frac{-\omega_m^2 ct}{a^2}\right)\right),\\
v(y,t) &= \frac{F}{Ga}\left(\frac{(\nu-1)y}{2} - (\nu_u - 1)y\sum_{m=1}^{\infty}\frac{\sin(\omega_m)\cos(\omega_m)}{\omega_m - \sin(\omega_m)\cos(\omega_m)}\exp\left(-\frac{\omega_m^2 ct}{a^2}\right)\right),\\
p(x,t) &= \frac{2FB(1+\nu_u)}{3a}\sum_{m=1}^{\infty}\frac{\sin(\omega_m)}{\omega_m - \sin(\omega_m)\cos(\omega_m)}\left(\cos\left(\frac{\omega_m x}{a}\right) - \cos(\omega_m)\right)\exp\left(-\frac{\omega_m^2 ct}{a^2}\right),
\end{aligned}
\tag{56}
$$

where ω_m are positive roots of

$$
\cos(\omega_m) - \frac{\nu_u - \nu}{1-\nu}\frac{\sin\omega_m}{\omega_m} = 0. \tag{57}
$$

The initial guess for the i-th root is $\omega_m = \pi/2 + \pi m$ which is then refined using the Newton method. The initial pressure and displacements satisfying (56) are given by

$$
u(x,0) = \frac{F\nu_u x}{2Ga}, \quad v(y,0) = \frac{F(\nu_u - 1)y}{2Ga}, \quad p(x,0) = \frac{FB(1+\nu_u)}{3a}. \tag{58}
$$

Force F applied to the impermeable rigid plate implies the integral constraint at the top boundary

$$
\int\limits_{\partial\Omega\cup\{y=b\}} \mathrm{d}\mathbf{S}^T\mathbf{t}_{\mathbb{B}} = \sum_{f\in(\partial\Omega\cup\{y=b\})} |f|\mathbf{n}^T\mathbf{t}_{\mathbb{B}} = Fa^2, \tag{59}
$$

that is added to the system and requires introduction of unknown Lagrangian multiplier λ. The boundary conditions at the top side $\partial\Omega\cup\{y=b\}$ are $\Gamma_R^m \cup \Gamma_N^f$ with $\gamma_\perp = \lambda$, where λ is the Lagrange multiplier for the additional constraint (59). With this condition the vertical movement of the rigid plate is constrained by the total force it applies on a sample. The initial value for λ is taken from the reference solution $v(b,0)$. On the right side $\partial\Omega\cup\{x=a\}$ the boundary conditions are $\Gamma_N^m \cup \Gamma_D^f$ with $\mathbf{F} = \mathbf{0}$ and $p_b = 0$. On the rest of the boundary the impermeable roller boundary conditions are imposed $\Gamma_R^m \cup \Gamma_N^f$. Medium properties are given in Table 5. The setup is illustrated in Fig. 4 (left). The problem parameters are $a = 1$, $b = 2$, $F = 10$.

We consider two types of grids: $N \times 2N \times 1$ cubical grid and $2N \times 2N \times 1$ prismatic grid. The prismatic grid is obtained by splitting each cube of the cubic grid into two prisms with alternating direction. The convergence of the discrete solution at $T = 20$ is shown in Table 6. The first order convergence is due to the Backward Euler method used for the approximation of the time derivative in the Biot term. The Mandel-Cryer effect of non-monotonic (in time) pressure behavior is displayed in Fig. 4 (right). The oscillations and their stabilization are demonstrated in Fig. 5 where a small time step is performed on the finest cubic grid.

Table 6
Error norms at $T = 20$ for the test in § 5.3.

Cubic grid				Prismatic grid			
$\lvert\mathcal{V}(\Omega)\rvert$	Δt	ε_u	ε_p	$\lvert\mathcal{V}(\Omega)\rvert$	Δt	ε_u	ε_p
$8 \times 16 \times 1$	0.2	4.7e-4	6.9e-3	$2 \cdot 8 \times 16 \times 1$	0.2	3.6e-4	8.5e-3
$16 \times 32 \times 1$	0.1	1.8e-4	4.0e-3	$2 \cdot 16 \times 32 \times 1$	0.1	1.6e-4	4.4e-3
$32 \times 64 \times 1$	0.05	7.9e-5	2.1e-3	$2 \cdot 32 \times 64 \times 1$	0.05	7.6e-5	2.3e-4
rate	-	1.19	0.9	rate	-	0.97	1.08

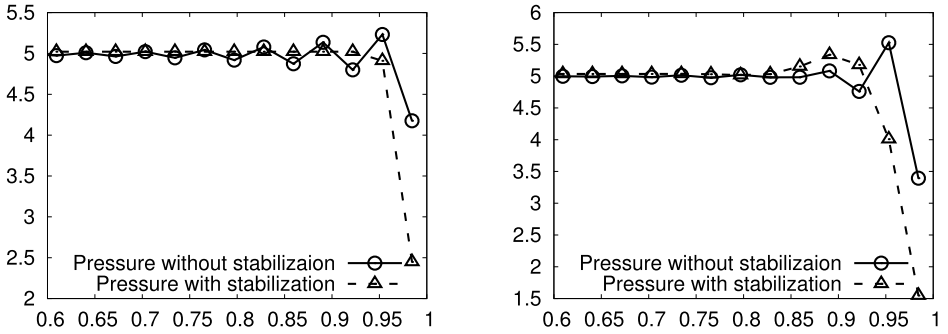

Fig. 5. Oscillatory (non-stabilized) and non-oscillatory (stabilized) discrete pressure solution in Mandel's problem § 5.3 on $32 \times 64 \times 1$ cubic grid with time step size $\Delta t = 10^{-4}$ at $T = 10^{-4}$ (left) and $T = 10^{-3}$ (right), horizontal axis corresponds to coordinate $x \in [0.6, 1]$, vertical axis corresponds to fluid pressure.

Table 7
Parameters for the test in § 5.4.

E	ν	k	α	$1/M$	μ	g
1000	0.25	0.01	1	0	1	0

5.4. Barry & Mercer problem

Next we consider the Barry & Mercer problem with pulsating source [54] with a known analytical solution. The solution is given in two dimensions. We set a problem in the unit cube $\Omega = [0, 1]^3$. The medium is isotropic and homogeneous. The stiffness tensor C is given by Young modulus E and Poisson's ratio ν, the Biot tensor and the permeability tensor are given by $\mathbb{B} = \alpha\mathbb{I}$, $\mathbb{K} = k\mathbb{I}$, respectively, where α is the Biot coefficient and k is the permeability parameter. The parameters are given in Table 7. The source term is given by

$$q = \beta \sin(\omega\theta t)\delta(x - x_0)\delta(y - y_0), \quad (x_0, y_0, z_0)^T = (1/4, 1/4, 1/2)^T, \tag{60}$$

where $\delta(\cdot)$ is the Dirac function, $\theta = kE(1-\nu)/(1+\nu)/(1-2\nu)$ and $\beta = 0.1$, $\omega = 1$. The total simulation time is $T = 1.2$.

Analytical solution is given in terms of double summation:

$$\begin{aligned}
g_{ij}(t) &= -\frac{\beta \sin(\lambda_i x_0)\sin(\lambda_j y_0)}{\theta\left(\lambda_{ij}^2 + \omega^2\right)}\left(\lambda_{ij}\sin(\omega\theta t) - \omega\cos(\omega\theta t) + \omega e^{-\lambda_{ij}\theta t}\right),\\
u(x, y, t) &= -4\sum_{i=1}^{\infty}\sum_{j=1}^{\infty}\frac{\lambda_i}{\lambda_{ij}} g_{ij}(t)\cos(\lambda_i x)\sin(\lambda_j y),\\
v(x, y, t) &= -4\sum_{i=1}^{\infty}\sum_{j=1}^{\infty}\frac{\lambda_j}{\lambda_{ij}} g_{ij}(t)\sin(\lambda_i x)\cos(\lambda_j y),\\
p(x, y, t) &= \frac{4E(1-\nu)}{(1+\nu)(1-2\nu)}\sum_{i=1}^{\infty}\sum_{j=1}^{\infty} g_{ij}(t)\sin(\lambda_i x)\sin(\lambda_j y),
\end{aligned} \tag{61}$$

where $\lambda_i := \pi i$, $\lambda_j := \pi j$, $\lambda_{ij} := \lambda_i^2 + \lambda_j^2$. The summation is computed to the accuracy of the terms 10^{-7} with the limitation $i^2 + j^2 < 2 \cdot 500^2$. The initial conditions are zero pressure and displacement.

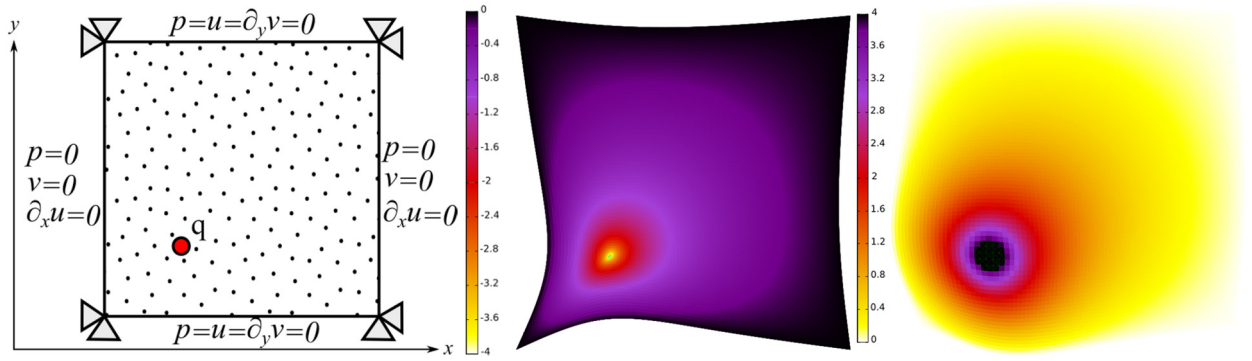

Fig. 6. Boundary conditions in the Barry & Mercer problem (left) in § 5.4, the pressure solution at time $T = 0.4$ (middle) and $T = 0.65$ (right) on the $94 \times 94 \times 1$ grid distorted by the magnified displacement $400 \cdot \mathbf{u}$. (For interpretation of the colors in the figure(s), the reader is referred to the web version of this article.)

Table 8
Error norms for the test in § 5.4.

$\lvert\mathcal{V}(\Omega)\rvert$	Δt	ε_u	ε_p
$10 \times 10 \times 1$	0.08	6.3e-6	5.7e-1
$22 \times 22 \times 1$	0.04	1.7e-6	2.0e-1
$46 \times 46 \times 1$	0.02	6.5e-7	7.2e-2
$94 \times 94 \times 1$	0.01	2.9e-7	2.3e-2
rate	-	1.14	1.61

The boundary conditions are shown in Fig. 6. The conditions at the boundary part $\partial\Omega \cap (\{x = 0\} \cup \{y = 0\} \cup \{x = 1\} \cup \{y = 1\})$ are given by $\Gamma_T^m \cup \Gamma_D^f$. At the boundary part $\partial\Omega \cap (\{z = 0\} \cup \{z = 1\})$ we set impermeable roller boundary conditions $\Gamma_R^m \cup \Gamma_N^f$.

We consider a set of refined cubical grids of the size $N \times N \times 1$, where $N \in \{10, 22, 46, 94\}$ and corresponding time step size $\Delta t = \{0.08, 0.04, 0.02, 0.01\}$. The choice of N is guided by the position of the source. The convergence of the discrete solution due to the stabilized method is demonstrated in Table 8. Higher than the first order convergence rate is observed. The reduction of convergence rate from the second order is attributed to the first order Backward Euler time integration formula.

5.5. Mandel's problem with transversely isotropic material

Mandel's problem with a transversely isotropic material was suggested in [55]. The problem provides an analytical solution for transversely isotropic Biot tensor. The setup is similar to § 5.3 except that we swap y and z directions and the domain is $\Omega = [0, a] \times [0, a] \times [0, b]$ with $a = 1$ and $b = 2$, see Fig. 7 (left). The material properties are described by Young modulii $E_x = E_y$, E_z, Poisson's ratios $\nu_{xy} = \nu_{yz}$, ν_{xz}, shear modulii $G_{xz} = G_{yz}$, $G_{xy} = \frac{E_x}{2(1+\nu_{xy})}$, solid and fluid bulk modulii K_s, K_f, porosity ϕ. The permeability is given by $\mathbb{K} = \operatorname{diag}(k_x, k_y, k_z)$ with $k_x = k_y$. The Biot coefficient $\mathbb{B} = \operatorname{diag}(\alpha_x, \alpha_y, \alpha_z)$ and the Biot modulus M are defined by components of 6×6 stiffness tensor $C = \{c_{ij}\}_{1 \le i,j \le 6}$ in Voigt notation by

$$\alpha_x = \alpha_y = 1 - \frac{c_{11} + c_{12} + c_{13}}{3K_s}, \quad \alpha_z = 1 - \frac{2c_{13} + c_{33}}{3K_s}, \quad M = \frac{K_s}{1 + \phi\left(\frac{K_s}{K_f} - 1\right) - \frac{2c_{11}+c_{33}+2c_{12}+4c_{13}}{9K_s}}, \tag{62}$$

where the solid bulk modulus is

$$K_s = \frac{3}{(1 - 2\nu_{xy} - 2\nu_{xz})/E_x + (1 - 2\nu_{yz})/E_y + 1/E_z}. \tag{63}$$

The analytical solution is defined in terms of the following coefficients:

$$c = \frac{k_x M c_{11}}{\mu\left(c_{11} + \alpha_x^2 M\right)}, \quad A_1 = \frac{\alpha_x^2 c_{33} - 2\alpha_x \alpha_z c_{13} + \alpha_z^2 c_{11}}{\alpha_z c_{11} - \alpha_x c_{13}} + \frac{c_{11}c_{33} - c_{13}^2}{M(\alpha_z c_{11} - \alpha_x c_{13})}, \quad A_2 = \frac{\alpha_z c_{11} - \alpha_x c_{13}}{c_{11}}. \tag{64}$$

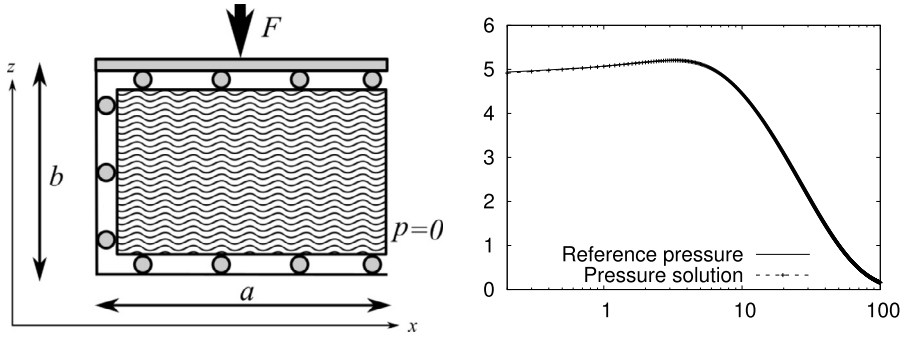

Fig. 7. Setup of Mandel's problem with transversely isotropic material (left) in § 5.5. Reproduction of the Mandel-Cryer effect of non-monotone pressure behavior over time period $T = 100$ with $\Delta t = 0.1$ at the left side of the $8 \times 1 \times 16$ cubic mesh, horizontal axis corresponds to time in log scale, vertical axis corresponds to fluid pressure (right).

Table 9
Independent parameters for the test in § 5.5.

E_x	E_z	ν_{xy}	ν_{xz}	G_{xz}	k_x	k_z	μ	ϕ	K_f
2.5	1.5	0.15	0.35	2	10^{-4}	10^{-7}	10^{-2}	0.5	1.5

Table 10
Error norm at $T = 20$ for the test in § 5.5.

Cubic grid				Prismatic grid			
$\lvert\mathcal{V}(\Omega)\rvert$	Δt	ε_u	ε_p	$\lvert\mathcal{V}(\Omega)\rvert$	Δt	ε_u	ε_p
$8 \times 1 \times 16$	0.2	7.9e-3	1.2e-2	$2 \cdot 8 \times 1 \times 16$	0.2	5.1e-3	9.6e-3
$16 \times 1 \times 32$	0.1	2.5e-3	4.5e-3	$2 \cdot 16 \times 1 \times 32$	0.1	1.8e-3	3.8e-3
$32 \times 1 \times 64$	0.05	9.0e-4	1.9e-3	$2 \cdot 32 \times 1 \times 64$	0.05	7.4e-4	1.7e-3
rate	-	1.47	1.25	rate	-	1.31	1.19

The analytical pressure and displacements are

$$
\begin{aligned}
p(x,t) &= \frac{2F}{aA_1}\sum_{m=1}^{\infty}\left(\cos\left(\frac{\omega_m x}{a}\right)-\cos(\omega_m)\right)\frac{\sin(\omega_m)}{\omega_m-\sin(\omega_m)\cos(\omega_m)}\exp\left(-\frac{\omega_m^2 ct}{a^2}\right),\\
u(x,t) &= \frac{Fx}{a}\frac{c_{13}}{c_{11}c_{33}-c_{13}^2}-\frac{2Fx}{a}\frac{\alpha_x\alpha_z M+c_{13}}{A_1M(\alpha_z c_{11}-\alpha_x c_{13})}\sum_{m=1}^{\infty}\frac{\cos(\omega_m)\sin(\omega_m)}{\omega_m-\sin(\omega_m)\cos(\omega_m)}\exp\left(-\frac{\omega_m^2 ct}{a^2}\right)\\
&\quad+\frac{2F\alpha_x}{A_2c_{11}}\sum_{m=1}^{\infty}\frac{\cos(\omega_m)\sin\left(\frac{\omega_m x}{a}\right)}{\omega_m-\sin(\omega_m)\cos(\omega_m)}\exp\left(-\frac{\omega_m^2 ct}{a^2}\right),\\
w(z,t) &= -\frac{Fz}{a}\frac{c_{11}}{c_{11}c_{33}-c_{13}^2}\left(1+2\left(\frac{A_2}{A_1}-1\right)\sum_{m=1}^{\infty}\frac{\cos(\omega_m)\sin(\omega_m)}{\omega_m-\sin(\omega_m)\cos(\omega_m)}\exp\left(-\frac{\omega_m^2 ct}{a^2}\right)\right).
\end{aligned}
\tag{65}
$$

The initial pressure and displacements are

$$
\begin{aligned}
p(x,0) &= \frac{F}{aA_1},\\
u(x,0) &= \frac{Fx}{a}\left(\frac{c_{13}}{c_{11}c_{33}-c_{13}^2}+\frac{a\alpha_x}{(A_1-A_2)c_{11}}-\frac{A_2\left(\alpha_x\alpha_z M+c_{13}\right)}{(A_1-A_2)A_1M(\alpha_z c_{11}-\alpha_x c_{13})}\right),\\
w(z,0) &= -\frac{Fz}{a}\frac{(A_1-A_2)c_{11}}{A_1\left(c_{11}c_{33}-c_{13}^2\right)}.
\end{aligned}
\tag{66}
$$

The boundary conditions are similar to the ones in § 5.3. The medium properties are given in Table 9. The other parameters are $K_s = 3.8136$, $\alpha_x = 0.6239$, $\alpha_y = 0.7109$, $M = 2.6779$.

We consider the $N \times 1 \times 2N$ cubic grid and the $2N \times 1 \times 2N$ prismatic grid. The convergence of the discrete solution at $T = 20$ is presented in Table 10. The method properly handles the transversely isotropic material.

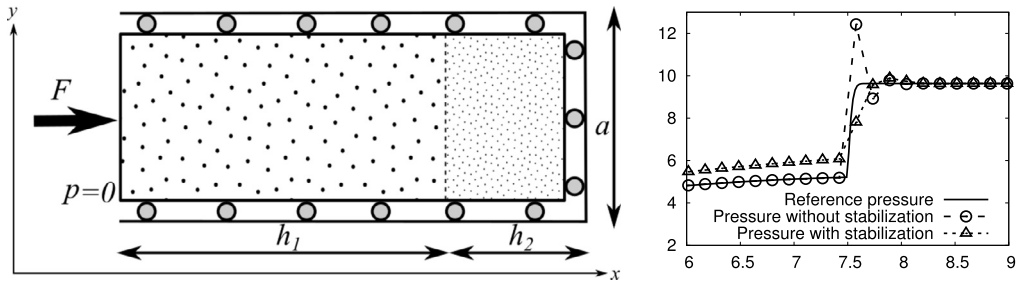

Fig. 8. Setup of Terzaghi's problem with two materials (left) in § 5.6. Impact of the stabilization method on the grid $64 \times 1 \times 1$ and time step $\Delta t = 40$ near the point of material discontinuity at $T = 600$, horizontal axis corresponds to coordinate $x \in [6, 9]$, vertical axis corresponds to fluid pressure (right).

5.6. Terzaghi's problem in two-layered medium

The pressure solution to the F-loaded consolidation of a column consisting of two materials of height h_1 and h_2, is given in [52] (page 44). The problem provides an analytical solution for a discontinuous Biot coefficient. The setup and boundary conditions are similar to the ones in § 5.2. We derive the displacement by integrating the strain from the bottom to x. For $\xi := h_1 - x$, $\xi \in [-h_2, h_1]$ the analytical solution reads as

$$
\begin{aligned}
g_m(t) &= \frac{2BF}{\omega_m} \frac{\exp\left(-\omega_m^2 c_2 t / h_2^2\right)}{(1+\beta\theta)\cos(\theta\omega_m)\sin(\omega_m) + (\beta+\theta)\sin(\theta\omega_m)\cos(\omega_m)}, \\
p(\xi, t) &= \sum_{m=0}^{\infty} g_m(t) \begin{cases} \cos(\omega_m)\cos\left(\theta\omega_m \xi / h_1\right) - \beta \sin(\omega_m)\sin\left(\theta\omega_m \xi / h_1\right), & \xi > 0, \\ \cos(\omega_m)\cos\left(\omega_m \xi / h_2\right) - \sin(\omega_m)\sin\left(\omega_m \xi / h_2\right), & \xi < 0. \end{cases} \\
u(\xi, t) &= F \begin{cases} m_1 \xi + m_2 h_2, & \xi > 0, \\ m_2(\xi + h_2), & \xi < 0. \end{cases} \\
&\quad - \sum_{m=0}^{\infty} \frac{g_m(t)}{\theta\omega_m} \begin{cases} \alpha_1 m_1 h_1 \left(\cos(\omega_m)\sin\left(\theta\omega_m \xi / h_1\right) + \beta \sin(\omega_m)\cos\left(\theta\omega_m \xi / h_1\right)\right) \\ \qquad -\alpha_1 m_1 h_1 \beta \sin(\omega_m) + \alpha_2 m_2 h_2 \theta \sin(\omega_m), & \xi > 0, \\ \alpha_2 m_2 h_2 \theta \left(\cos(\omega_m)\sin\left(\omega_m \xi / h_2\right) + \sin(\omega_m)\cos\left(\omega_m \xi / h_2\right)\right), & \xi < 0. \end{cases}
\end{aligned}
\tag{67}
$$

The Skempton's coefficients B_i, the consolidation coefficients c_i and the confined compressibility coefficients m_i are given by

$$
B_i = \frac{\alpha_i m_i M_i}{1 + \alpha_i^2 m_i M_i}, \quad c_i = \frac{k_i}{\mu} \frac{M_i}{1 + \alpha_i^2 m_i M_i}, \quad m_i = \frac{(1+\nu)(1-2\nu)}{E(1-\nu)}, \tag{68}
$$

where k_i is the permeability, E_i is the Young modulus, ν_i is the Poisson's ratio and μ is the fluid viscosity.

Parameter M_2 is chosen so that $B_1 = B_2 = B$. The expressions for M_2 and coefficients β and θ are

$$
M_2 = \frac{\alpha_1 m_1}{\alpha_2 m_2} \frac{M_1}{1 + \alpha_1 m_1 (\alpha_1 - \alpha_2) M_1}, \quad \beta = \frac{k_2}{k_1}\frac{c_1}{c_2}, \quad \theta = \frac{h_1}{h_2}\sqrt{\frac{c_2}{c_1}}. \tag{69}
$$

Coefficients $\omega_m = \bar{\omega}_m / (1+\theta)$ and $\bar{\omega}_m$ are the positive roots of the equation

$$
\cos(\bar{\omega}_m) - \frac{\beta - 1}{\beta + 1} \cos\left(\frac{\theta - 1}{\theta + 1}\bar{\omega}_m\right) = 0. \tag{70}
$$

The trigonometric problem (70) is solved using the combination of the Newton's method with the golden ratio line search method starting from the initial guess $\bar{\omega}_m = \pi/2 + m\pi$.

The initial pressure and displacement are given by:

$$
p(\xi, 0) = BF, \quad u(\xi, 0) = F \begin{cases} m_1(1 - \alpha_1 B)\xi + m_2(1 - \alpha_2 B)h_2, & \xi > 0, \\ m_2(1 - \alpha_2 B)(\xi + h_2), & \xi < 0. \end{cases} \tag{71}
$$

The setup is illustrated in Fig. 8 (left). The heights and material properties for each layer are given in Table 11. The width is $a = 1$. We consider a set of $N \times 1 \times 1$ cubical grids. The instability develops near the point of material discontinuity even for large time step $\Delta t = 40$ and is successfully suppressed by the stabilization method, see Fig. 8 (right). The stabilized solution on the coarse $64 \times 1 \times 1$ grid at different time instants is demonstrated in Fig. 9. The analytical solution develops into a step near the point of material discontinuity and thus challenges the numerical method. The proposed method without stabilization with the same parameters develops oscillations near the point of discontinuity as displayed in Fig. 10 and diverges. The convergence of the stabilized discrete solution is reported in Table 12.

Table 11
Heights and material parameters for the test in § 5.6.

Material	h	E	ν	k	α	M	μ
1	7.5	10	0.45	10^{-5}	1	1000	10^{-2}
2	2.5	2	0.15	10^{-8}	0.8	by equation (69)	

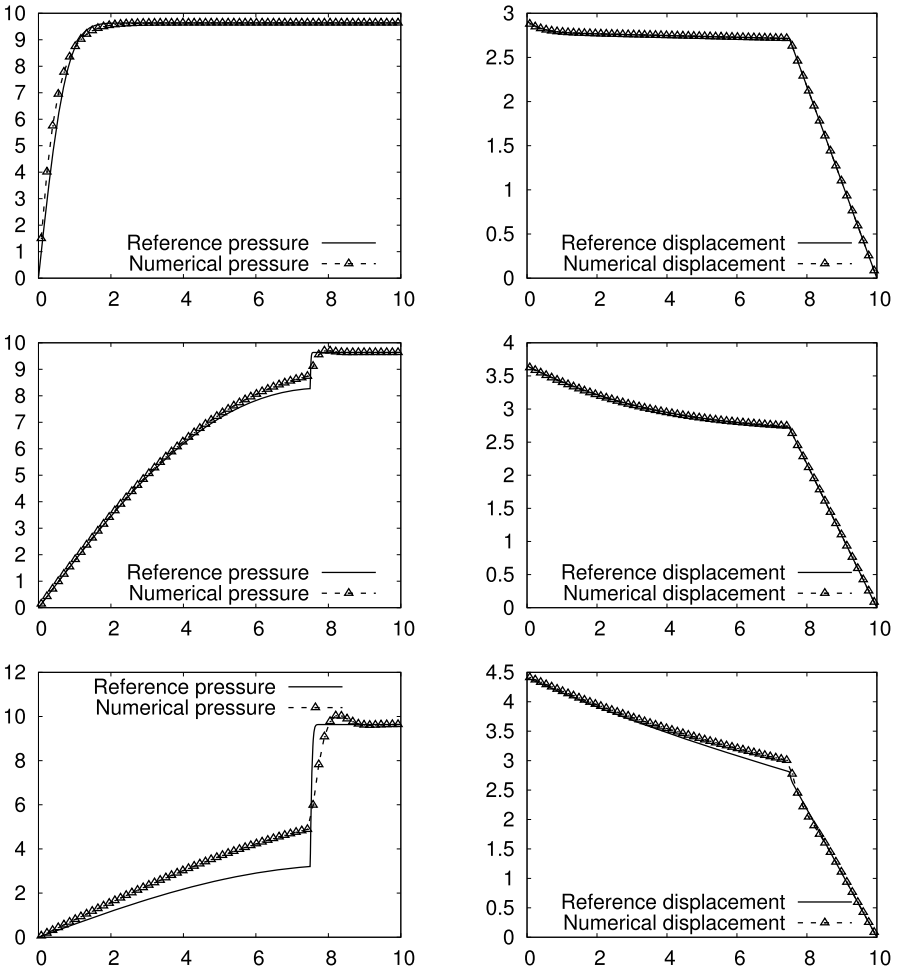

Fig. 9. Pressure (left) and displacement (right) at vertical axis against coordinate $x \in [0, 10]$ at horizontal axis for Terzaghi's problem in two-layered medium § 5.6 at time instants $T = 5$ (top), $T = 250$ (middle) and $T = 1000$ (bottom) on the $64 \times 1 \times 1$ grid with time step $\Delta t = 5$.

Table 12
Error norms at $T = 1000$ for the test in § 5.6.

$\lvert\mathcal{V}(\Omega)\rvert$	Δt	ε_u	ε_p
$64 \times 1 \times 1$	4	9.6e-01	8.5e-2
$128 \times 1 \times 1$	2	6.2e-01	5.1e-2
$256 \times 1 \times 1$	1	3.6e-01	2.4e-2
$512 \times 1 \times 1$	0.5	1.7e-01	8.2e-3
rate	-	1.03	1.57

5.7. Norne formation

The presented method is capable to handle general polyhedral grids demanded in engineering applications. The open porous media initiative [56] provides grid data of the Norne oil field featuring faults, pinch-outs and heterogeneity. The diagonal permeability tensor $\mathbb{K} = \operatorname{diag}(K_x, K_y, K_z)$ and porosity data ϕ are taken from the grid data. The permeability is isotropic in horizontal direction, $K_x = K_y$. A mild vertical anisotropy is defined with the net-to-gross thickness ratio parameter [57].

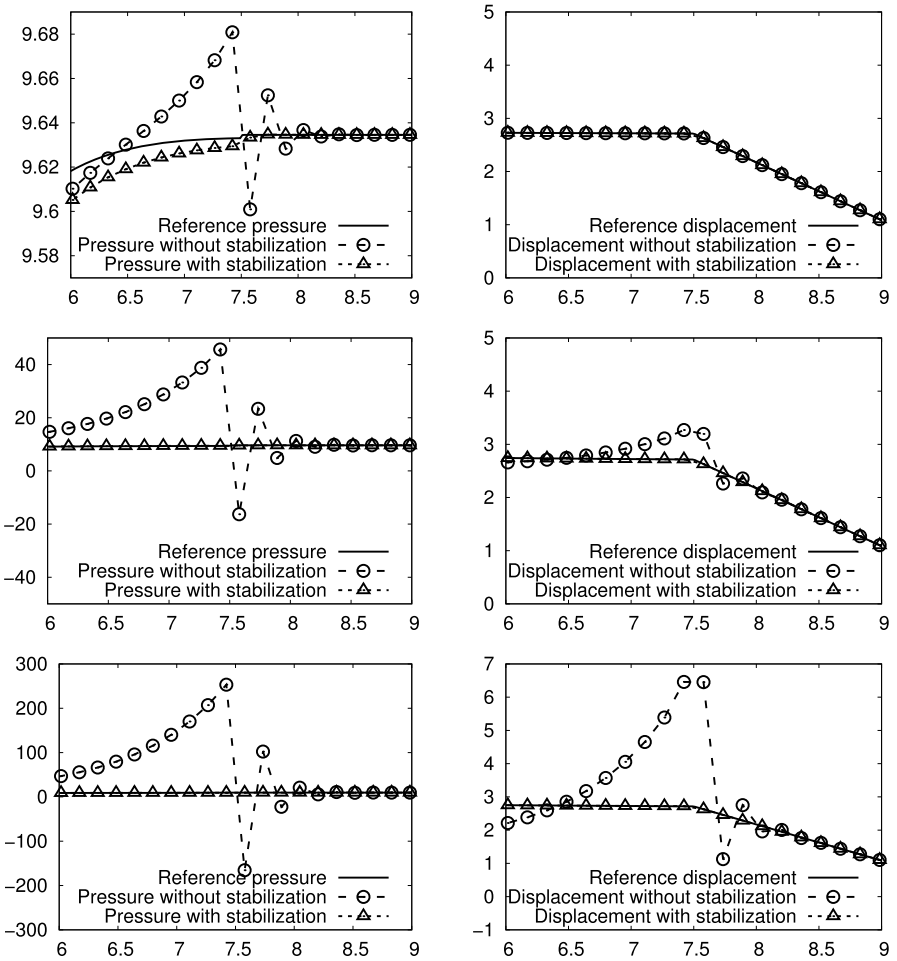

Fig. 10. Pressure (left) and displacement (right) at vertical axis against coordinate $x \in [6, 9]$ at horizontal axis for Terzaghi's problem in two-layered medium § 5.6 at time instants $T = 50$ (top), $T = 125$ (middle) and $T = 150$ (bottom) on the $64 \times 1 \times 1$ grid with time step $\Delta t = 5$.

Table 13
Properties of the wells in § 5.7.

Well	x_W	y_W	z_W	WI	p_{bhp}
1	4.567151e+5	7.321079e+6	2.767665e+3	500000	300000
2	4.609346e+5	7.323503e+6	2.597767e+3	500000	1000
3	4.595400e+5	7.326078e+6	2.803586e+3	500000	0

We define the mechanical properties from the permeability and porosity. The Biot coefficient is $\mathbb{B} = \frac{1}{2}(1+\phi)\mathbb{I}$ and the mechanical material properties are $E_x = 5000(\bar{K}_x + 1)$, $E_y = 5000(\bar{K}_y + 1)$, $E_z = 5000(\bar{K}_z + 1)$, $G_{yz} = 2500(\bar{K}_x + 1)$, $G_{xz} = 2500(\bar{K}_y + 1)$, $G_{xy} = 2500(\bar{K}_z + 1)$, $\nu_{xy} = \nu_{xz} = 1/10$, $\nu_{yz} = 1/5$. Here $\bar{K}_\alpha = (K_\alpha - \min(K_\alpha))\,/\,(\max(K_\alpha) - \min(K_\alpha))\,, \forall \alpha \in \{x, y, z\}$. The other coefficients are $\rho_f = 20$, $\rho_s = 120$, $M = 2(1+\phi)$, $\mu = 0.1$, $g = -9.8$. These parameters are synthetic and are not tied to real physical properties.

The impermeable roller boundary condition $\Gamma_R^m \cup \Gamma_N^f$ is imposed on the entire boundary $\partial\Omega$. The initial conditions corresponds to pressure at 250 and zero displacement. The flow is driven by three wells with properties collected in Table 13 (left). Positions of the wells in the reservoir are illustrated in Fig. 11. The well contributes to the right hand side:

$$q = \frac{WI}{\mu}\left(p - p_{bhp}\right)\delta(\mathbf{x} - \mathbf{x}_W). \tag{72}$$

We integrated the problem (1) till $T = 100$ with the time step $\Delta t = 1$. Fig. 11 demonstrates the pressure field (middle) and the displacement magnitude (right) at the final time $T = 100$.

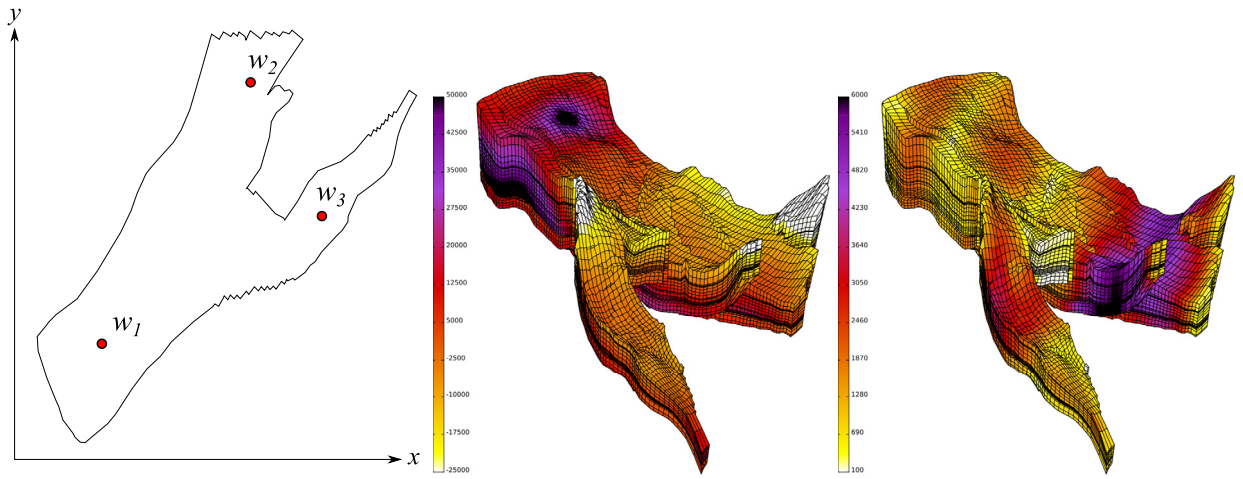

Fig. 11. Top view of the wells positions in the outline of the Norne oil field (left). Pressure (middle) and displacement magnitude (right) at time $T = 100$ in the problem § 5.7, scaled by 6 in vertical direction.

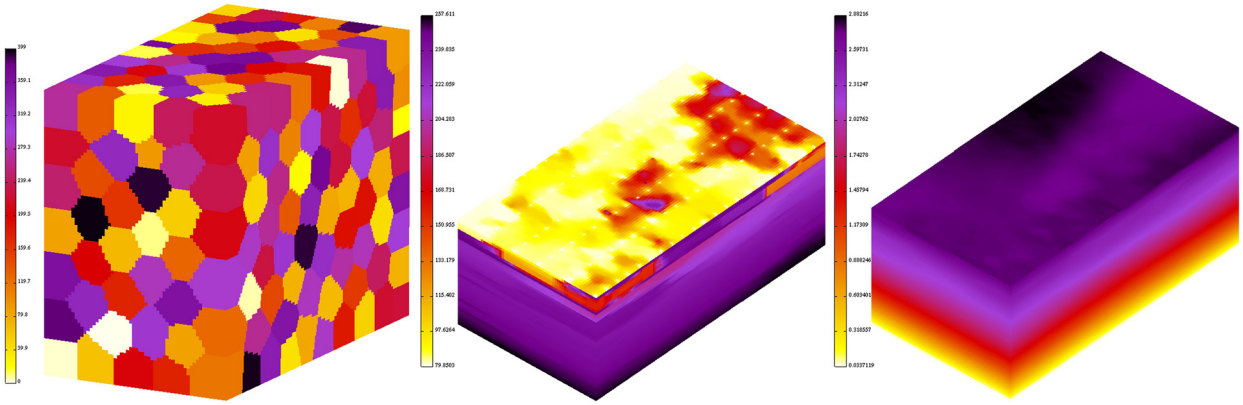

Fig. 12. Mesh distribution among 400 processors with the K-means method (left). Pressure in the cutaway of the grid at $z = 170$ (middle) and displacement magnitude in the cutaway of the grid at $z = 190$ (right) at time $T = 100$ in the problem § 5.8.

5.8. SPE10 dataset

We consider a larger SPE10 dataset [58] to evaluate the parallel performance of the simulator. The dataset contains $60 \times 220 \times 85$ entries of porosity and components of diagonal permeability tensor with strong vertical anisotropy. We define the mechanical properties and other parameters following the approach from § 5.7 except the gravity $g = -0.01$, in order to account for the vertical anisotropy. The problem is set on a regular $60 \times 220 \times 85$ cartesian grid in the domain $\Omega = [0, 240] \times [0, 440] \times [0, 340]$. The initial and boundary conditions are similar to the problem from § 5.7.

The flow is guided by 132 wells with $WI = 500000$ and $p_{bhp} = 80$. The positions of wells are given by

$$\mathbf{x}_{ij} = \left(2 + (i-1)\frac{236}{5}, 1 + (j-1)\frac{438}{21}, 170\right), \forall i \in [1, 6], \forall j \in [1, 22]. \tag{73}$$

The mesh is distributed in advance with the K-means clustering algorithm described in [59]. The mesh distribution among 400 processors is illustrated in Fig. 12 (left). The problem is integrated with the time step $\Delta t = 1$ till $T = 100$. The pressure and displacement magnitude at the final time step are presented in Fig. 12 (middle, right). The simulator performance on two parallel computers is collected in Fig. 12. The machines are the Lomonosov supercomputer [60,61] and the INM RAS cluster [62]. At the Lomonosov supercomputer we have a limit of 50 nodes with 14 core processors. In the table N_{proc} is the number of processors, T_{tot} is the total simulation time including input-output and synchronization barriers, T_{asm} is the matrix assembly time, T_{prec} is the preconditioner preparation, T_{iter} is the time needed for the linear iterations, T_{upd} is the solution update and recomputation of gradients and interface values. The total number of unknowns in the linear system is 4 488 000. (See Table 14.)

Table 14
Solver scalability in problem § 5.8, the time is given in seconds.

Machine	N_{proc}	T_{tot}	T_{asm}	T_{prec}	T_{iter}	T_{upd}
INM RAS cluster	100	15079.4	1119.8	7245.2	4463	479.7
	200	8791.2	582.9	3926.2	2800.9	252.4
	400	4637	300.3	1965.6	1374.2	127
Lomonosov supercomputer	175	13298	798.7	6807.9	3779.5	361
	350	6397.3	460.4	2111.1	2177.4	138.4
	700	3536	234.1	1071.1	1112.4	70.5

6. Conclusion

The presented cell-centered finite-volume method is applicable for the poromechanics problem characterized by heterogeneous full tensor coefficients: the permeability tensor, the Biot coefficient tensor and the elasticity stiffness tensor. The cornerstone of the method is the stable discretization of the coupled vector flux and derivation of the harmonic point providing interpolation across material discontinuities.

The stabilization method proposed in this work addresses the inf-sup instability issue. The hourglass oscillation pattern is replaced with a smooth kink in the discrete solution. The presence of the kink indicates that the scheme may still suffer in the presence of sharp steps in the solution. To address these issues, the future research will be directed towards a nonlinear finite-volume extension of the method.

CRediT authorship contribution statement

Kirill M. Terekhov: Conceptualization, Funding acquisition, Methodology, Software, Validation, Visualization, Writing – original draft. **Yuri V. Vassilevski:** Conceptualization, Formal analysis, Methodology, Supervision, Writing – review & editing.

Declaration of competing interest

The authors declare that they have no known competing financial interests or personal relationships that could have appeared to influence the work reported in this paper.

Acknowledgement

This work was supported by the Russian Science Foundation through the grant 21-71-20024 (the finite volume method, its stabilization and parallel implementation), and 19-71-10094 (method verification on the analytical solutions and poroelastic deformation benchmarks). The research is carried out using the equipment of the shared research facilities of HPC computing resources at Lomonosov Moscow State University.

References

[1] M. Biot, General theory of three-dimensional consolidation, J. Appl. Phys. 12 (2) (1941) 155–164.
[2] D. Keyes, L. McInnes, C. Woodward, W. Gropp, E. Myra, M. Pernice, J. Bell, J. Brown, A. Clo, J. Connors, et al., Multiphysics simulations: challenges and opportunities, Int. J. High Perform. Comput. Appl. 27 (1) (2013) 4–83.
[3] O. Coussy, Poromechanics, John Wiley & Sons, 2004.
[4] E. Detournay, A.-D. Cheng, Fundamentals of poroelasticity, in: Analysis and Design Methods, Elsevier, 1993, pp. 113–171.
[5] T. Garipov, M. Karimi-Fard, H. Tchelepi, Discrete fracture model for coupled flow and geomechanics, Comput. Geosci. 20 (1) (2016) 149–160.
[6] N. Castelletto, G. Gambolati, P. Teatini, A coupled MFE poromechanical model of a large-scale load experiment at the coastland of Venice, Comput. Geosci. 19 (1) (2015) 17–29.
[7] P. Teatini, M. Ferronato, G. Gambolati, M. Gonella, Groundwater pumping and land subsidence in the Emilia-Romagna coastland, Italy: modeling the past occurrence and the future trend, Water Resour. Res. 42 (1) (2006).
[8] B. Jha, R. Juanes, Coupled multiphase flow and poromechanics: a computational model of pore pressure effects on fault slip and earthquake triggering, Water Resour. Res. 50 (5) (2014) 3776–3808.
[9] S. Badia, A. Quaini, A. Quarteroni, Coupling Biot and Navier–Stokes equations for modelling fluid–poroelastic media interaction, J. Comput. Phys. 228 (21) (2009) 7986–8014.
[10] S. Dana, M. Wheeler, Convergence analysis of fixed stress split iterative scheme for anisotropic poroelasticity with tensor Biot parameter, Comput. Geosci. (2018) 1–12.
[11] T. Garipov, M. Hui, et al., Simulation of coupled geomechanics and multiphase flow in naturally fractured reservoirs, in: 52nd US Rock Mechanics/Geomechanics Symposium, American Rock Mechanics Association, 2018.
[12] O. Zienkiewicz, et al., The Finite Element Method, vol. 3, McGraw-Hill, London, 1977.
[13] K. Aziz, A. Settari, Petroleum Reservoir Simulation, Applied Science Publishers, 1979, https://books.google.com/books?id=GJ5TAAAAMAAJ.
[14] A. Settari, K. Aziz, et al., Use of irregular grid in reservoir simulation, Soc. Pet. Eng. J. 12 (02) (1972) 103–114.
[15] T. Garipov, M. Zaslavsky, A. Pergament, Mathematical modeling of filtration processes and poro-elasticity, Mat. Model. 17 (9) (2005) 113–128.
[16] R. Dean, X. Gai, C. Stone, S. Minkoff, et al., A comparison of techniques for coupling porous flow and geomechanics, SPE J. 11 (01) (2006) 132–140.
[17] S. Dana, M. Wheeler, Convergence analysis of two-grid fixed stress split iterative scheme for coupled flow and deformation in heterogeneous poroelastic media, Comput. Methods Appl. Mech. Eng. 341 (2018) 788–806.

[18] J. Kim, H. Tchelepi, R. Juanes, Stability and convergence of sequential methods for coupled flow and geomechanics: fixed-stress and fixed-strain splits, Comput. Methods Appl. Mech. Eng. 200 (13–16) (2011) 1591–1606.
[19] I. Sokolova, H. Hajibeygi, Multiscale finite volume method for finite-volume-based poromechanics simulations, in: ECMOR XVI-16th European Conference on the Mathematics of Oil Recovery, 2018.
[20] N. Castelletto, J.A. White, M. Ferronato, Scalable algorithms for three-field mixed finite element coupled poromechanics, J. Comput. Phys. 327 (2016) 894–918.
[21] B. Ganis, R. Liu, B. Wang, M. Wheeler, I. Yotov, Multiscale modeling of flow and geomechanics, Radon Ser. Comput. Appl. Math. (2013) 165–204.
[22] J. Nordbotten, Stable cell-centered finite volume discretization for Biot equations, SIAM J. Numer. Anal. 54 (2) (2016) 942–968.
[23] M. Preisig, J. Prévost, Stabilization procedures in coupled poromechanics problems: a critical assessment, Int. J. Numer. Anal. Methods Geomech. 35 (11) (2011) 1207–1225.
[24] C. Rodrigo, F. Gaspar, X. Hu, L. Zikatanov, Stability and monotonicity for some discretizations of the Biot's consolidation model, Comput. Methods Appl. Mech. Eng. 298 (2016) 183–204, https://doi.org/10.1016/j.cma.2015.09.019, http://www.sciencedirect.com/science/article/pii/S0045782515003138.
[25] H. Honório, C. Maliska, M. Ferronato, C. Janna, A stabilized element-based finite volume method for poroelastic problems, J. Comput. Phys. 364 (2018) 49–72, https://doi.org/10.1016/j.jcp.2018.03.010, http://www.sciencedirect.com/science/article/pii/S0021999118301621.
[26] K. Terekhov, Y. Vassilevski, Finite volume method for coupled subsurface flow problems, I: Darcy problem, J. Comput. Phys. 395 (2019) 298–306.
[27] A. Léo, E. Robert, H. Raphaèl, A Nine-Point Finite Volume Scheme for the Simulation of Diffusion in Heterogeneous Media, Comptes Rendus Mathematique, vol. 347, Elsevier France, Paris, 2009, pp. 673–676.
[28] K. Terekhov, B. Mallison, H. Tchelepi, Cell-centered nonlinear finite-volume methods for the heterogeneous anisotropic diffusion problem, J. Comput. Phys. 330 (2017) 245–267.
[29] K. Terekhov, H. Tchelepi, Cell-centered finite-volume method for elastic deformation of heterogeneous media with full-tensor properties, J. Comput. Appl. Math. 364 (2020) 112331.
[30] K.M. Terekhov, Multi-physics flux coupling for hydraulic fracturing modelling within inmost platform, Russ. J. Numer. Anal. Math. Model. 35 (4) (2020) 223–237.
[31] K. Terekhov, Cell-centered finite-volume method for heterogeneous anisotropic poromechanics problem, J. Comput. Appl. Math. 365 (2020) 112357.
[32] Y. Vassilevski, K. Terekhov, K. Nikitin, I. Kapyrin, Parallel Finite Volume Computation on General Meshes, Springer International Publishing, 2020.
[33] K. Terekhov, Collocated finite-volume method for the incompressible Navier-Stokes problem, J. Numer. Math. 29 (1) (2020) 63–79.
[34] K.M. Terekhov, Fully-implicit collocated finite-volume method for the unsteady incompressible Navier–Stokes problem, in: Numerical Geometry, Grid Generation and Scientific Computing, Springer, 2021, pp. 361–374.
[35] P. Bonnet, X. Ferrieres, B. Michielsen, P. Klotz, J. Roumiguières, Finite-Volume Time Domain Method, Academic Press, San Diego, CA, 1999.
[36] C. Oosterlee, H. Ritzdorf, Flux difference splitting for three-dimensional steady incompressible Navier–Stokes equations in curvilinear co-ordinates, Int. J. Numer. Methods Fluids 23 (4) (1996) 347–366.
[37] E.F. Toro, Riemann Solvers and Numerical Methods for Fluid Dynamics: a Practical Introduction, Springer Science & Business Media, 2013.
[38] R. Eymard, T. Gallouët, R. Herbin, Finite volume methods, Handb. Numer. Anal. 7 (2000) 713–1018.
[39] R.H. Rand, Introduction to maxima, Cornel Univ. 25 (2005) 22.
[40] K. Terekhov, Y. Vassilevski, Inmost parallel platform for mathematical modeling and applications, in: Russian Supercomputing Days, Springer, 2018, pp. 230–241.
[41] A. Danilov, K. Terekhov, I. Konshin, Y. Vassilevski, Parallel software platform INMOST: a framework for numerical modeling, Supercomput. Front. Innov. 2 (4) (2016) 55–66.
[42] I. Konshin, I. Kapyrin, K. Nikitin, K. Terekhov, Application of the parallel inmost platform to subsurface flow and transport modelling, in: Parallel Processing and Applied Mathematics, Springer, 2016, pp. 277–286.
[43] Y. Vassilevski, I. Konshin, G. Kopytov, K. Terekhov, INMOST - a Software Platform and a Graphical Environment for Development of Parallel Numerical Models on General Meshes, Moscow State Univ. Publ, Moscow, 2013.
[44] G. Sleijpen, H. Van der Vorst, D. Fokkema, Bicgstab (l) and other hybrid bi-cg methods, Numer. Algorithms 7 (1) (1994) 75–109.
[45] I. Kaporin, High quality preconditioning of a general symmetric positive definite matrix based on its UTU + UTR + RTU - decomposition, Numer. Linear Algebra Appl. 5 (6) (1998) 483–509.
[46] N. Li, Y. Saad, E. Chow, Crout versions of ILU for general sparse matrices, SIAM J. Sci. Comput. 25 (2) (2003) 716–728.
[47] K. Terekhov, Parallel multilevel linear solver within inmost platform, in: Russian Supercomputing Days, Springer, 2020, pp. 297–309.
[48] M. Bollhöfer, A robust ILU with pivoting based on monitoring the growth of the inverse factors, Linear Algebra Appl. 338 (1) (2001) 201–218.
[49] M. Olschowka, A. Neumaier, A new pivoting strategy for Gaussian elimination, Linear Algebra Appl. 240 (1996) 131–151.
[50] H.F. Wang, Theory of Linear Poroelasticity with Applications to Geomechanics and Hydrogeology, Princeton University Press, 2017.
[51] V.E. Borisov, A.V. Ivanov, B.V. Kritsky, I.S. Menshov, E.B. Savenkov, Numerical modelling of poroelasticity problems, Preprints Keldysh Institute of Applied Mathematics RAS (0) 81–36, 2017 (in Russian).
[52] A. Verruijt, Theory and Problems of Poroelasticity, Delft University Press, 2016, https://geo.verruijt.net/software/PoroElasticity2016b.pdf.
[53] A.H.-D. Cheng, E. Detournay, A direct boundary element method for plane strain poroelasticity, Int. J. Numer. Anal. Methods Geomech. 12 (5) (1988) 551–572.
[54] S.I. Barry, G.N. Mercer, Exact solutions for two-dimensional time-dependent flow and deformation within a poroelastic medium, J. Appl. Mech. 66 (2) (1999) 536–540.
[55] Y. Abousleiman, A.-D. Cheng, L. Cui, E. Detournay, J.-C. Roegiers, Mandel's problem revisited, Geotechnique 46 (2) (1996) 187–195.
[56] B. Flemisch, K. Flornes, K. Lie, A. Rasmussen, Opm: the open porous media initiative, in: AGU Fall Meeting Abstracts, 2011.
[57] G. Schlumberger, Eclipse Reference Manual, Schlumberger, Houston, TX, 2014.
[58] M.A. Christie, M. Blunt, Tenth SPE comparative solution project: a comparison of upscaling techniques, SPE Reserv. Eval. Eng. 4 (04) (2001) 308–317.
[59] K. Terekhov, Parallel dynamic mesh adaptation within inmost platform, in: Russian Supercomputing Days, Springer, 2019, pp. 313–326.
[60] V. Sadovnichy, A. Tikhonravov, V. Voevodin, V. Opanasenko, "Lomonosov": supercomputing at Moscow state university, in: Contemporary High Performance Computing, Chapman and Hall/CRC, 2017, pp. 283–307.
[61] V.V. Voevodin, A.S. Antonov, D.A. Nikitenko, P.A. Shvets, S.I. Sobolev, I.Y. Sidorov, K.S. Stefanov, V.V. Voevodin, S.A. Zhumatiy, Supercomputer Lomonosov-2: large scale, deep monitoring and fine analytics for the user community, Supercomput. Front. Innov. 6 (2) (2019) 4–11.
[62] Inm ras cluster, https://cluster2.inm.ras.ru/en/.